# Shared Transcriptomic Signatures Reveal Synaptic Pruning as a Link Between Alzheimer's Disease and Epilepsy

Huihong Li[1,2,3], Jianwei Li[1,2,3,4], Mingjie Chen[5], Xueke Liu[5], Yushan Sun[5], Jie Wu[1,2,3], Bingying Lin[1,2,3,4], Si Chen[1,2,3,4], Zihan Deng[1,2,3,4], Mengqi Hong[1,2,3,4], Nai-Li Wei[1], Xiaoyu Ji[1,2,3,4*]

[1]Department of Neurosurgery, The First Affiliated Hospital of Shantou University Medical College, Shantou, Guangdong 515041, China

[2]Brain Function and Disease Laboratory, Shantou University Medical College, Shantou, Guangdong 515041, China

[3]Department of Pharmacology, Shantou University Medical College, Shantou, Guangdong, 51504, China

[4]Pain and Related Diseases Research Laboratory, Shantou University Medical College, Shantou, Guangdong 515041, China

[5]Department of Biotechnology and Food Engineering, Guangdong Technion – Israel Institute of Technology, Shantou, China 515063.

[*]**Corresponding authors**
Contact: Dr. Xiaoyu Ji, xyji@stu.edu.cn;

**Keywords:** Alzheimer's disease, epilepsy, synaptic pruning, neurodegeneration, transcriptome, Tyrobp, Trem2, C1q

**Abstract**

The mechanism of epileptogenesis in Alzheimer's disease (AD) remains poorly understood, though growing evidence indicates shared molecular mechanisms between epilepsy (EP) and AD. This study aims to reveal these overlapping molecular mechanisms by reanalyzing two extensive bulk RNA-seq datasets: one from a pilocarpine-induced temporal lobe epilepsy (TLE) model (n=200) and the other from AD models, specifically rTg4510 (TG) tauopathy and J20 amyloidosis (n=141). We identified 101 differentially expressed genes (DEGs) shared between EP and the tauopathy model, though none were shared between EP and the amyloidosis model. These shared DEGs were significantly enriched in immune-related terms. Weighted gene co-expression network analysis (WGCNA) revealed a highly preserved immune module strongly associated with both EP and tauopathy models, which also significantly overlapped with modules constructed from EP and AD human patient datasets. This module contained 19 shared hub genes enriched in the synapse pruning biological process, with shared regulatory network analysis revealing a pathway where Tyrobp regulates C1q component genes through Trem2. Cell composition deconvolution showed decreased neuronal and increased microglial composition in both EP and tauopathy models, with strong correlations observed between these cellular composition changes and the expression of shared hub genes. Further validation using single-cell/nucleus sequencing data from EP and AD patients confirmed a high microglia-specific expression of key genes, including Tyrobp, Trem2, and C1q components, in both EP and AD patients relative to other hub genes. These findings suggest that immune-related processes, particularly microglial-mediated synaptic pruning, are essential in both disorders and may drive neurodegeneration and epileptogenesis.

## Graphic abstract

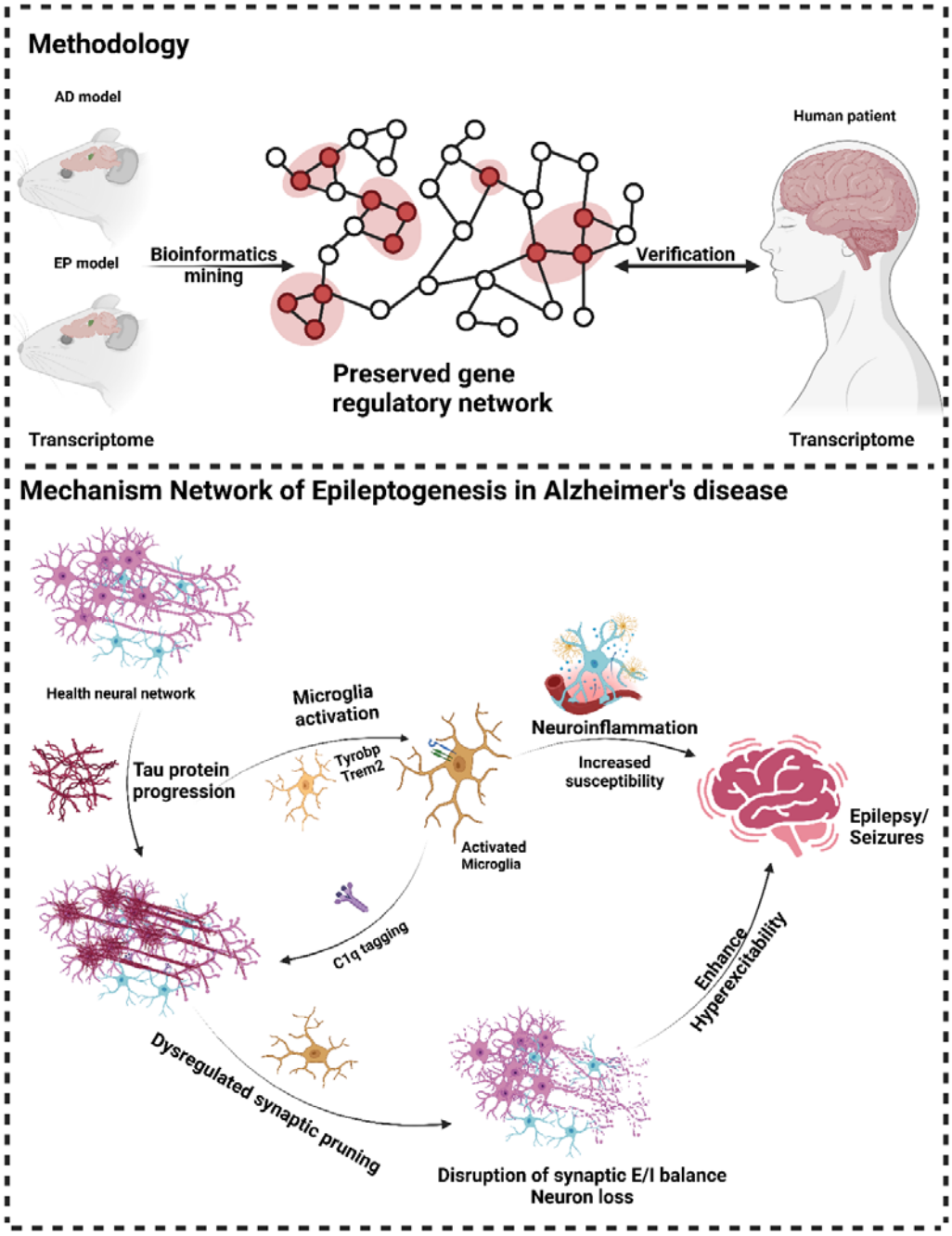

## 1. Introduction

Alzheimer's disease (AD) and epilepsy (EP) are increasingly recognized for their complex, bidirectional relationship, particularly in the elderly [1–3]. AD, the most common form of dementia, affects approximately 36 million people worldwide, with cases expected to triple by 2050 due to rising life expectancy [4]. While the accumulation of amyloid-beta (Aβ) and tau proteins has long been central to AD pathology [5], recent studies have also highlighted the contribution of neuroimmune, inflammatory mechanisms, and neurochemical imbalances in disease progression [6,7]. Epilepsy, a neurological disorder characterized by recurrent, unprovoked seizures, affects over 70 million people globally, with notably high incidence among the elderly, especially those with neurodegenerative conditions such as AD [8,9]. Despite advances in treatment options, both diseases still face challenges in effective treatment and a complete understanding of their underlying causes [10–12].

Accumulating evidence suggests that AD contributes to a higher risk of epilepsy. Epidemiological studies indicate that individuals with AD have a significantly higher likelihood of developing epilepsy, with 10–22% experiencing unprovoked seizures and 22–54% showing subclinical epileptiform activity [13,14]. Conversely, people with EP are at heightened risk for cognitive impairment and dementia, underscoring a bidirectional relationship between these conditions [15]. Both diseases share overlapping pathological features particularly temporal lobe epilepsy (TLE), including amyloid deposition, tau pathology, and hippocampal sclerosis [16–18]. Additionally, AD transgenic animal models display spontaneous seizures and increased susceptibility to epilepsy, suggesting that AD's pathology may promote and trigger epileptic activity [19–22].

Previous research suggests that the accumulation of tau and Aβ proteins may contribute not only to the neurodegeneration characteristic of AD but also to the increased seizure susceptibility observed in these patients [1,23–25]. Shared genetic factors between AD and EP have also been identified, especially mutations in the presenilin 1 gene, which is involved in amyloid plaque formation in AD [26]. Additionally, common proteomic signatures in the brains of EP and AD patients were found to be associated with tau protein [13]. People with epilepsy, especially those with TLE, have been found to have higher levels of phosphorylated tau aggregates than age-matched controls [13]. The shared genetic, molecular, and pathological features between AD and EP suggest that therapeutic strategies targeting these common pathways could benefit both conditions.

Recent advances in genomics, transcriptomics, and proteomics have revealed AD and EP comorbidity through data from patient cohorts and animal models [13,27]. However, significant gaps remain in our understanding of the mechanisms driving this comorbidity [3]. Treating EP in AD patients is further complicated by potential drug

interactions and adverse effects [28,29]. A systems biology approach is urgently needed to comprehensively explain the shared molecular mechanisms and cellular processes underlying these conditions. Taking full advantage of large-scale transcriptomic data from models and patients and integrating multi-omics analyses, we can deepen our understanding of their pathophysiology and accelerate the discovery of novel therapeutic targets and biomarkers for early diagnosis and treatment monitoring [30].

We hypothesize that there are conserved molecular pathways in both EP and AD models, as well as in human patients. To test this, we conducted a comprehensive analysis and integration of large-scale transcriptomic data from AD tau/Aβ models, EP models, and human patient datasets to identify common transcriptomic signatures, cellular dynamics, and shared pathways involved in both diseases. We found that conserved transcriptomic signatures were notably present in both EP and AD with tauopathy, particularly in immune-related processes. Specifically, hub genes such as Tyrobp, Trem2, and C1q component genes, involved in microglia-mediated synaptic pruning, emerged as key shared signatures.

## 2. Materials and Methods

### 2.1 Data Collection

We downloaded and reanalyzed two extensive bulk RNA-seq datasets from mouse models to investigate the potential mechanisms of epileptogenesis in AD. The EP dataset, obtained from the European Nucleotide Archive (PRJEB18790), includes bulk RNA-seq data from 200 hippocampi of pilocarpine TLE model mice and healthy control [31]. The AD dataset, sourced from the Gene Expression Omnibus (GSE125957), comprises bulk RNA-seq data from 141 samples of the entorhinal cortex and hippocampus of AD model mice that expressed either human tau (rTg4510, TG) or amyloid precursor protein (J20) and their corresponding healthy controls at various ages (2, 4, 6, 8, 10, and 12 months) [32].

To verify the clinical relevance of our findings from mouse models, we further retrieved publicly available microarray datasets, including 129 hippocampal samples from TLE patients (GSE63808) and 97 middle temporal gyrus samples from AD patients (GSE132903) [33,34]. Additionally, we integrated single-cell sequencing (scRNA-Seq) data from 85,780 immune cells from six drug-refractory EP patients (GSE201048) and single-nucleus sequencing (snRNA-Seq) data from 174,420 immune cells of 217 AD patients and 226 controls (GSE227223) [35,36].

### 2.2 Quality control and preprocessing

All the downloaded raw RNA sequences were processed for quality check and trimmed to acquire clean sequences using FastQC and Fastp with stringent parameters (--qualified_quality_phred 30 --n_base_limit 5 --detect_adapter_for_pe --cut_tail

--trim_front1 15 --dedup --trim_poly_x --trim_poly_g) to ensure high data quality [37,38]. Ribodetector was used to remove potential rRNA contamination [39]. Low-quality regions in the sequences, attributed to instability in the sequencing platform, were also trimmed using Fastp. Trimmed sequences were then aligned to the GRCm39.111 reference mouse genome using HISAT2 [40] and followed by quantification using featureCounts [41].

For the AD dataset, samples were excluded from subsequent analysis based on the criteria outlined in the original publication, resulting in 121 high-quality RNA-seq samples. For the EP dataset, duplicate and low-quality samples were initially removed. Then a variance-stabilizing transformation was applied to the count matrix before performing Principal Component Analysis (PCA) to identify potential outlier samples. PCA was then performed to identify outliers, with Mahalanobis distances calculated from PCA scores. A chi-squared distribution threshold of 0.975 was used to detect significant outliers, resulting in 11 samples subsequently excluded from analysis (**Fig. S1**). Detailed information on quality control and mapping metrics is provided in **Table S1**.

Following quality control, mapping, and exclusion of low-quality samples, we achieved an average of 61.30 million (SD = 22.78 million) sequencing reads per sample for the EP dataset and 22.20 million (SD = 6.56 million) sequencing reads per sample for the AD dataset. No significant differences in read depth were observed between model groups and wild-type (WT) controls (EP: two-tailed unpaired t-test, $t[171] = 1.01$, $p = 0.31$; TG: two-tailed unpaired t-test, $t[55] = 1.35$, $p = 0.18$; J20: two-tailed unpaired t-test, $t[60] = 0.78$, $p = 0.43$).

### 2.3 Differential Expression Analysis

Differential expression analysis was conducted using DESeq2 [42]. Before analysis, non-expressed and lowly expressed genes were filtered out. For the EP dataset, only genes with at least 20 counts in a minimum of 90 samples (~90 samples per group) were retained, while for the AD dataset, genes with at least 20 counts in at least 6 samples (6–8 samples per group) were kept. The DESeq function was then used to estimate size factors and dispersions and to perform statistical testing for differential expression [42].

For the EP dataset, the design formula was specified as ~Condition (EP/WT), and results were extracted by comparing the "EP" condition to the "WT" condition. For the AD dataset, we aimed to detect progressive differentially expressed genes (DEGs), following a previous approach [32], using DESeq's likelihood-ratio test to fit the statistical model: $Gene\ expression = Genotype + Age + Genotype \times Age$ (Interaction). P-values were adjusted for multiple testing using the Benjamini-Hochberg (BH) correction.

DEGs were identified based on an adjusted p-value < 0.05 and |log2 fold change| > 1. These thresholds were applied to the EP dataset and to the final time point of the AD dataset. Shared DEGs between the EP and AD datasets were identified by taking the intersection of their DEG results. Kyoto Encyclopedia of Genes and Genomes (KEGG) pathway and gene ontology (GO) analyses for shared DEGs were performed using WebGestalt, with weighted set cover redundancy removal [43].

**2.4 Weighted Gene Co-expression Network Construction**

To construct weighted gene co-expression networks and compare results from EP and AD datasets, we employed a standard meta-WGCNA comparison method [44–46]. All datasets underwent variance-stabilizing transformation using DESeq2 to normalize the variance across different samples. We then calculated the median absolute deviation (MAD) and retained the top 85% of genes with the highest MAD in each dataset, resulting in 10,997 genes common to all datasets for comparability in further analyses. Outliers were identified through hierarchical clustering, excluding two samples from the rTg4510 dataset and three from the J20 dataset (**Fig. S2**). To assess dataset comparability, general network properties such as average gene expression and overall network connectivity were calculated (**Fig. S3**).

We constructed signed co-expression networks using the WGCNA R package [45], selecting the lowest soft-thresholding power of 9 to achieve a scale-free topology fit index (R^2) of at least 0.85 across datasets (**Fig. S3**). Adjacency matrices were generated using the signed network option and converted to topological overlap matrices (TOM) to quantify similarity in gene connectivity profiles. Modules were identified by average linkage hierarchical clustering of TOM dissimilarity (1-TOM), followed by dynamic tree cutting with parameters deepSplit = 2 and minClusterSize = 24. This procedure was also applied to patient microarray datasets, using variance-stabilizing normalization with the “limma” package (**Fig. S4A-C**) [47].

To match modules between EP and AD networks, we used the matchModules function [44], which maps AD network module colors to best-matching EP modules based on a hypergeometric test. Module profiles were summarized using module eigengenes (MEs), derived from the first principal component of each module. To identify modules significantly associated with disease genotypes (EP or interaction of TG/J20), we calculated Pearson correlation coefficients between MEs and genotype information, with significance defined as $p < 0.05$ and an absolute correlation coefficient > 0.65 [48]. Module membership (MM) and gene-genotype significance (GS) were also determined by calculating Pearson correlations between individual genes and MEs or genotypes, respectively. KEGG pathway and GO analyses for module annotation were conducted using WebGestalt with weighted set cover redundancy removal [43].

## 2.5 Module Preservation Analysis

To assess module preservation of EP module in AD datasets, we used two approaches [49]: Zsummary preservation statistics and cross-tabulation-based preservation statistics.

We employed the modulePreservation function from the WGCNA R package, with parameters set to networkType="signed", nPermutations=100, to calculate composite Z-summary preservation statistics. This metric evaluates preservation based on module size, network density, and connectivity, offering a comprehensive assessment of how well the structure of EP modules is maintained in AD datasets. The Z-summary thresholds were interpreted as follows: Z-summary > 10 indicates strong evidence of preservation, 2 < Z-summary < 10 suggests moderate evidence, and Z-summary < 2 indicates no evidence of preservation [49]. To complement the Z-summary statistic, we also used the medianRank preservation statistic, which assesses relative preservation across modules with less dependency on module size. A lower median rank denotes stronger observed preservation [49].

Additionally, we used a cross-tabulation method to examine module overlap between EP and AD datasets, as well as between mouse model and patient datasets (**Fig. S4D-E**). This method generates a contingency table reporting the overlapping gene number between each module in the reference and test datasets. The statistical significance of overlaps was assessed using Fisher's exact test, with p-values adjusted using the BH correction. A module was considered significantly overlapping if the overlap count was > 30 and the adjusted p-value was < 0.05.

## 2.6 Hub Gene Identification and Network Analysis

Hub genes likely to act as key drivers within a module were identified using stringent criteria to minimize false positives: genes ranking in the top 10% for intramodular connectivity within each module, MM > 0.9, and GS > 0.4. Shared hub genes were determined by intersecting the hub genes of key modules in both EP and AD datasets, along with the DEGs.

To further explore interactions and potential regulatory relationships among shared hub genes in the EP and AD datasets, we constructed a protein-protein interaction (PPI) network using the STRING database with a confidence score threshold of 0.4 and a false discovery rate (FDR) of 5% (https://string-db.org/cgi/input.pl) [50]. This network was visualized using NetworkAnalyst [51]. We then performed regulatory network analysis with the GENIE3 algorithm (default parameters), which applies a random forest approach to infer potential regulatory relationships from gene expression data. GENIE3 ranks regulatory interactions by weight, with higher weights indicating stronger regulatory links [52].

Gene expression profiles of the key module from the EP and TG datasets were used to infer plausible regulatory interactions among shared hub genes. To reduce false positives, a weight threshold of 0.01 was applied to filter out weaker regulatory links. Additionally, only the top 30 plausible regulatory links between shared hub genes were retained to construct gene regulatory networks. Finally, the shared regulatory network of hub genes was constructed by intersecting the regulatory networks inferred from the EP and TG datasets and visualized using NetworkAnalyzer in Cytoscape [53].

### 2.7 Cell Composition Deconvolution

In silico deconvolution can estimate the cellular composition of a tissue sample from its gene expression profile, with CIBERSORT particularly suited for cellular composition deconvolution of brain transcriptomes [54,55]. The raw count expression matrix was converted to FPKM values using edgeR [56], followed by cell composition deconvolution using CIBERSORT via the BrainDeconvShiny platform, with cell-type signatures specific to *Mus musculus* from immunopurified mouse brain tissue [55,57].

For statistical analysis, the Mann-Whitney test ($p < 0.05$) was applied to compare the EP dataset with the control group, while the Kruskal-Wallis test was used for the AD datasets, followed by pairwise comparisons across age and genotype groups. The BH method was used to control the FDR ($q < 0.05$). Associations between identified cell types and shared hub genes or modules were determined by calculating Pearson correlation coefficients.

### 2.8 Single-cell and Single-nucleus RNA Sequencing Analysis

Single-cell and single-nucleus RNA sequencing (sc/snRNA-seq) count matrices were downloaded and processed according to the methods outlined in the original publications [35,36,58]. Quality control was performed by filtering cells with high mitochondrial content (>20% for the EP dataset and >5% for the AD dataset) and selecting cells based on cellular complexity (300–5,000 genes per cell for the EP dataset and >500 genes for the AD dataset). Subsequent data processing was conducted using the standard Seurat pipeline, including scaling, normalization, variable gene identification, and clustering.

PCA was performed on the 2,000 most variable genes, with the first 20 principal components (PCs) used for t-SNE and clustering in the EP dataset, and the first 30 PCs used for the AD dataset. Cluster identities were determined by identifying DEGs with the FindMarkers function, followed by annotation based on the original publications. For the AD dataset, only single nuclei from AD patients were used for visualizing expression distributions of shared hub genes across clusters.

## 3. Results

## 3.1 Identification and Functional Enrichment of Shared DEGs

### 3.1.1 Differential Expression Analysis

To reveal the shared molecular signatures underlying EP and AD, we performed differential expression analysis using DESeq2. In the EP dataset, we identified 378 DEGs, with 351 upregulated and 27 downregulated genes (**Fig. 1A**). The TG dataset yielded 426 progressive DEGs, including 377 upregulated and 49 downregulated genes (**Fig. 1B**). In contrast, the J20 dataset contained only one upregulated progressive DEG, Cst7 (**Fig. 1C**). Notably, 101 genes were differentially expressed in both the EP and TG datasets, representing 26.72% and 23.71% of the DEGs in each dataset, respectively (**Fig. 1A–B**). This substantial overlap suggests shared molecular pathways between EP and TG models. Detailed DEG information is available in **Table S2**.

### 3.1.2 Functional Enrichment Analysis of Shared DEGs

To investigate the biological relevance of the shared DEGs, we conducted a functional enrichment analysis. KEGG pathway analysis identified several significantly enriched pathways, including “complement and coagulation cascades,” “phagosome,” and “cytokine-cytokine receptor interaction” (**Fig. 1D**). GO enrichment analysis highlighted key biological processes, such as “defense response,” “immune response,” and “regulation of cytokine production” (**Fig. 1E**). Additionally, enriched molecular functions included “signaling receptor binding” and “immune receptor activity,” with cellular components such as the “extracellular matrix” and “side of membrane” also significantly represented. These findings indicate that the shared DEGs are primarily involved in immune processes, potentially reflecting shared molecular pathways in both EP and TG models. Detailed GO enrichment analysis results can be found in **Table S2**.

## 3.2 Construction of Weighted Gene Co-Expression Network

WGCNA was particularly suited for this study due to its ability to identify modules of highly correlated genes, revealing underlying biological networks and pathways conserved across different conditions. By applying WGCNA to both EP and AD datasets, we aimed to identify conserved gene modules that may represent common molecular mechanisms between these neurological disorders.

### 3.2.1 Data preprocessing and Network comparability

After filtering out low-expression and low-variance genes in each dataset, we retained 10,997 genes common to all datasets for further analysis. For network construction, we selected a soft-thresholding power of 9 to ensure that networks in all datasets exhibited scale-free topology with a fit index > 0.85 (**Fig. S3A**). This threshold was consistently applied across analyses to maintain network comparability.

To assess comparability between EP and AD networks, we examined correlations of ranked mean gene expression and ranked gene connectivity between dataset pairs. For EP and J20, high correlations were observed for both expression ($r = 0.98$, $p < 1e\text{-}200$) and connectivity ($r = 0.23$, $p < 5.7e\text{-}132$). Similarly, EP and TG datasets showed significant correlations (expression: $r = 0.96$, $p = 1e\text{-}200$; connectivity: $r = 0.43$, $p = 1e\text{-}200$) (**Fig. S3B**), indicating comparability across datasets [44].

### 3.2.2 Module Construction

We used the WGCNA package to construct gene co-expression networks for the EP, TG, and J20 datasets. The analysis identified diverse gene modules across the three models: the EP dataset revealed 33 modules (28–790 genes per module) (**Fig. 2A**), TG had 29 modules (34–1,537 genes) (**Fig. 2B**), and J20 contained 32 modules (27–613 genes) (**Fig. 2C**). Detailed module information can be found in **Table S3**.

Associations between module eigengenes and model genotypes were assessed. The EP dataset identified seven modules significantly associated with the EP genotype: three with positive correlations (green, steelblue, turquoise; $0.73 \leq r \leq 0.79$, $p < 3e\text{-}31$) and four with negative associations (lightyellow, red, lightcyan, paleturquoise; $-0.92 \leq r \leq -0.69$, $p < 8e\text{-}27$). Notably, five of these modules contained DEGs linked to the EP genotype (turquoise: n=198, green: n=86, steelblue: n=12, lightcyan: n=12, red: n=5) (**Fig. 2A, D**), indicating potential roles in the EP model.

In the TG dataset, seven modules showed significant associations with the TG genotype: two with positive correlations (turquoise, yellow; $0.72 \leq r \leq 0.87$, $p < 3e\text{-}10$) and five with negative associations (brown, saddlebrown, darkorange2, darkmagenta, royalblue; $-0.83 \leq r \leq -0.67$, $p < 1e\text{-}08$). Nine modules contained DEGs associated with the TG genotype (turquoise: n=268, yellow: n=14, green: n=7, darkorange2: n=4, blue: n=2, orangered4: n=2, royalblue: n=2, darkmagenta: n=1, tan: n=1) (**Fig. 2B, E**), suggesting involvement in TG-specific pathways.

Consistent with DEG analysis, the J20 dataset showed fewer DEGs. No modules exhibited significant associations with the J20 genotype ($r < 0.4$) (**Fig. 2C, F**), aligning with prior studies that indicate minimal gene expression changes in this amyloid precursor protein model [32].

### 3.3 Module Preservation Analysis

Following module construction, we assessed the preservation of EP modules in the AD datasets to reveal molecular pathways potentially important to epileptogenesis in AD.

Our analysis revealed varying degrees of module preservation between EP and AD

datasets (**Fig. 3**). In the TG model, the steelblue module had low preservation scores (Z-summary.pres = 0.89, medianRank.pres = 33). Similarly, in the J20 model, the steelblue and yellow modules showed weak preservation (Z-summary.pres < 4), suggesting these may represent unique biological processes specific to the EP dataset. In contrast, several EP modules, including green, blue, and brown, exhibited high preservation scores and significant overlap with AD modules in both models, suggesting they represent conserved biological processes.

Notably, the turquoise EP module had the highest preservation scores (Z-summary.pres = 83.01, medianRank.pres = 12) and showed strong overlap with the TG turquoise module, displaying high overlap counts and the lowest adjusted p-values (**Fig. 3B-C**). Both turquoise modules were positively correlated with disease genotype (EP: r = 0.79, p = 5e-41; TG: r = 0.87, p = 4e-18) and contained most DEGs in each model (**Fig. 2A-B**). Other EP modules, such as lightcyan, showed significant correlations but did not display preservation. We further assessed the preservation of the mouse turquoise module in EP and AD patients, finding that the turquoise immune modules from EP and TG models significantly overlapped with modules constructed from EP and AD patient data, respectively (**Fig. S4D-E**). This suggests the turquoise module represents a conserved immune molecular signature across species and disease states, suggesting that immune processes play a preserved and significant role in these modules across conditions. Preservation statistics are shown in **Table S3**.

### 3.4 Shared Hub Gene Identification and Network Analysis

To identify hub genes that may play a crucial role in both EP and AD, we intersected the central genes of the turquoise module from EP and TG datasets with the previously identified 101 DEGs. This analysis identified 19 shared hub genes common to both conditions (**Fig. 4A-B**).

We constructed a PPI network to investigate the biological significance of these 19 genes **(Fig. 4C, Table S4**). The analysis revealed strong connectivity among C1q complex component genes (C1qa, C1qb, C1qc) and other immune-related genes, including Trem2, Tyrobp, and Adgre1. GO biological process enrichment analysis highlighted significant processes involving “synaptic pruning,” “immune effector process,” “complement activation, classical pathway,” “immunoglobulin-mediated immune response,” and “defense response” (**Fig. 4D, Table S4**). Genes involved in “synaptic pruning” (C1qc, C1qb, C1qa, Trem2) also participate in other enriched processes, such as “complement-mediated synapse pruning” (C1qa, Trem2) and “microglial cell activation” (Tyrobp, C1qa, Trem2) (**Table S4**).

While WGCNA reveals gene co-occurrence patterns, it does not identify regulatory mechanisms. To explain potential regulatory relationships among these 19 genes, we applied the GENIE3 algorithm to gene expression profiles of the turquoise module in

both EP and TG conditions (**Table S5**). By intersecting predicted regulatory networks from each condition, we identified a shared regulatory pathway: Tyrobp regulates Trem2, which in turn regulates the complement component C1q via C1qa (**Fig. 4E**).

These genes, particularly Tyrobp, Trem2, and C1q complex components (C1qa, C1qb, C1qc), play central roles in co-expression modules of both conditions and are involved in multiple enriched terms, especially synaptic pruning. Notably, these genes are also progressive DEGs in the TG model (**Fig. 4F, Fig. S5**). The successful reconstruction of a regulatory network involving Tyrobp, Trem2, and C1q suggests they represent a common molecular pathway underlying both conditions.

### 3.5 Cell Composition Deconvolution and Association with Shared Hub Gene

To investigate cellular composition changes and their associations with the 19 shared hub genes in TG and EP conditions, we employed CIBERSORT via BrainDeconvShiny for cell composition deconvolution of bulk RNA-seq data [54,55].

Our analysis revealed significant cellular composition alterations. Firstly, we observed a notable reduction in neuronal composition in both EP and TG conditions compared to controls (**Fig. 5A, B**). Secondly, there was a marked increase in microglial composition in both models, consistent with the enrichment of immune-related processes identified in previous analyses (**Fig. 5A, B**). While astrocyte and endothelial cell alterations were also detected in EP and TG models, these changes were less pronounced than the neuronal decrease and microglial increase observed in the TG model (**Fig. 5A, B**). No significant differences were found in oligodendrocyte composition in either condition.

We further examined the relationship between these cellular composition changes and the 19 shared hub genes by conducting Pearson correlation analyses (**Fig. 5C**). Notably, all 19 shared hub genes showed strong negative correlations with neuronal composition in both EP and TG conditions, suggesting an inverse relationship between their expression levels and neuronal proportion. Conversely, strong positive correlations were observed between the shared hub genes and microglial and endothelial cell composition. Correlations with astrocytes and oligodendrocytes were more variable and showed less consistency across genes and conditions.

Although no cellular composition changes were observed in the J20 model (**Fig. S6A**), we found that genes such as Tyrobp, Trem2, and C1q complex components, were strongly associated with microglial composition, indicating that these genes demonstrate a strong link with microglial cell types (**Fig. S6B**).

### 3.6 Localization and Validation Expression of Shared Hub Gene in Cell Types

To clarify the roles of shared hub genes in epileptogenesis within AD, we analyzed

their expression across cell types using the Whole Mouse Brain Transcriptomic Cell Type Atlas from the Allen Brain Atlas [59].

Among the 19 shared hub genes, the atlas indicated that most (15 of 19) were predominantly expressed in immune cells, particularly microglia and macrophages (**Fig. S7**). C4b and Gfap were primarily expressed in astrocytes, while Osmr was expressed in endothelial cells, pericytes, and smooth muscle cells. S100a6 showed broader expression across astrocytes, oligodendrocytes, and neurons (**Fig. S7**). Overall, these genes exhibited immune cell-specific expression, especially in microglia and macrophages.

To validate the cross-species relevance of these findings in humans, we analyzed sc/sn RNA-seq data from both EP and AD patient immune cells (**Fig. 6**). We found that 12 of the shared hub genes were detectable in both datasets. Among these, Tyrobp and Trem2, along with the C1q complex component genes, displayed notably high and predominant expression in microglia compared to other shared hub genes (**Fig. 6**). Additionally, Csf3r and Cxcl16 also showed strong microglial expression. Conversely, several genes, including Fcgr2b and Tgif1, were undetectable or exhibited low expression levels in immune cells from both patient groups (**Fig. 6**).

These findings confirmed the high and predominant expression of Tyrobp, Trem2, and C1q components genes in the microglia of both AD and EP patients. This consistency across animal models and human patients suggests the crucial role of microglia in the epileptogenesis of AD.

## 4. Discussion

AD and EP are increasingly recognized for their complex, bidirectional relationship. Despite this association, the molecular mechanisms linking AD and EP remain poorly understood. Previous research suggests that the accumulation of tau and Aβ proteins may contribute not only to the neurodegeneration characteristic of AD but also to the heightened seizure susceptibility observed in these patients [1,25].

This study aims to identify common molecular pathways underlying AD and EP by integrating data from experimental models and human patients. Using well-established AD mouse models with tau/Aβ pathology, EP mouse models, and gene expression data from human patients, we seek to shed light on shared molecular signatures and pathways that may drive both diseases.

### Immune Molecular Pathways Conserved in Epilepsy and Alzheimer's Disease

Our differential expression analysis revealed a significant overlap of 101 DEGs between the EP and TG models, representing 26.72% and 23.71% of the DEGs in

each dataset, respectively (**Fig. 1A-B**). This substantial overlap suggests shared molecular mechanisms between EP and AD, particularly those associated with tau pathology. The shared DEGs also highlight immune biomarkers common to both conditions, such as Cd68 and Gfap, markers of activated microglia and astrocytes, respectively [60,61]. In both AD and EP, microglial and astrocyte activation plays dual roles in disease progression: on the one hand, activated microglia can clear Aβ plaques, while reactive astrocytes provide metabolic support and maintain ion balance, potentially mitigating brain injuries or seizures [62,63]. However, chronic activation or dysfunction of these glial cells can perpetuate neuroinflammation, exacerbating Aβ accumulation, tau pathology, neuronal damage, and seizure activity [64–67].

Functional enrichment analysis of shared DEGs revealed significant involvement in immune-related pathways, underscoring the role of immune dysregulation in both EP and AD. GO and KEGG pathway analyses identified enrichment in processes and pathways associated with inflammation, including "immune response," "regulation of cytokine production," and "complement and coagulation cascades" (**Fig. 1D-E**).

Neuroinflammation has been implicated in the pathogenesis of both AD and EP, with shared inflammatory mechanisms contributing to disease progression [68–70]. Activation of microglia and astrocytes leads to the production of pro-inflammatory cytokines and chemokines, such as interleukin-1β (IL-1β), tumor necrosis factor-alpha (TNF-α), and interleukin-6 (IL-6). This not only contributes to neuronal hyperexcitability and increased seizure susceptibility but also exacerbates the accumulation and aggregation of Aβ and tau proteins, accelerating neurodegeneration and cognitive decline [68–70]. Beyond cytokines, other inflammatory components such as the complement system and blood-brain barrier (BBB) dysfunction are implicated in both diseases [71–74]. Activation of the complement cascade contributes to synaptic loss in AD and is observed in brain tissue from TLE patients [75–77]. BBB breakdown precedes neuronal hyperactivity in epilepsy, leading to astrocyte dysfunction and seizures [71]. In AD, BBB impairment facilitates the influx of peripheral inflammatory cells, exacerbating neuroinflammation [72].

Neuroinflammation may therefore represent a shared pathway that underlies the mutual influence of AD and EP [1,78]. In AD, inflammation can lead to neuronal hyperexcitability and increased seizure susceptibility, as seen in early-onset AD patients who have a higher prevalence of seizures [68,79]. Conversely, EP-induced inflammation may promote Aβ and tau accumulation, contributing to cognitive decline [65]. Cognitive impairment in TLE has been associated with Aβ and tau deposition, and anti-inflammatory treatments have been shown to reduce both neurodegeneration and seizure activity in EP models [80,81]. This bidirectional influence suggests a conserved immune network contributing to the pathologies of both AD and EP.

Our WGCNA analysis further supports immune system involvement, revealing the preservation of the immune-related turquoise module across both EP and TG models (**Fig. 2-3**). GO enrichment analysis confirmed that this module is heavily involved in immune functions linking the two disorders, including inflammatory response, glial cell activation, cytokine production, and blood vessel morphogenesis (**Table S3**). In addition, turquoise was the most significantly overlapping module when comparing co-expression networks from patient datasets. Previous studies on this dataset also reported significant overlap of this module across different AD patient studies, with several of our shared hub genes identified in both model and human patients [32]. Collectively, our results suggest that the turquoise immune module may represent a conserved pathology in humans, reinforcing the hypothesis that immune dysregulation is a core pathological feature in both AD and EP.

**Synaptic Pruning as a Central Interface between Epilepsy and Alzheimer's Disease**

Our analysis identified robust conservation of the turquoise module across both EP and TG datasets, indicating that shared hub genes may serve as key regulators in both conditions. Nineteen shared hub genes were identified, with GO enrichment and PPI analyses indicating "synaptic pruning" as the most significant biological process (**Fig. 4A-D**, **Table S4**). Key genes involved in this process—C1q complex components (C1qa, C1qb, C1qc), Trem2, and Tyrobp—were highly expressed in microglia from both AD and EP patient samples (**Fig. 4-6**).

Synaptic pruning is essential for refining neural circuits during development and maintaining synaptic homeostasis in the adult brain [82]. Microglia mediate this process by engulfing unnecessary synapses tagged by complement proteins such as C1q [83]. Microglial receptors like Trem2 and Tyrobp can recognize these tags to initiate phagocytosis [84,85]. Dysregulation or mutations in Tyrobp and Trem2 are associated with increased AD risk by impairing microglial function [85–87]. In AD, microglia surrounding amyloid plaques transition to a disease-associated microglia (DAM) state, characterized by enhanced phagocytic activity and elevated expression of genes like Tyrobp, Trem2, and Apoe, as well as complement proteins like C1q [85]. Loss of Tyrobp disrupts DAM activation, impairing microglial functions such as plaque clearance, which may increase the amyloid burden and worsen AD pathology [85,88].

Interestingly, Tyrobp deficiency can also confer resilience against synaptic dysfunction by reducing C1q accumulation, which is implicated in synaptic pruning and neurodegeneration [85,89]. It is already clear that C1q overexpression dysregulates synaptic pruning in elderly models and tauopathy models of AD, leading to pathological consequences [90–93]. C1q levels in the aged brain led to increased susceptibility to synaptic pruning, impairing synaptic plasticity and cognitive function.

By blocking C1q, researchers have observed improvements in synaptic function, memory retention, preserved cognition, and reduced neuroinflammation in aged animal models [91–95]. Recent studies indicate that Tyrobp plays a role in modulating C1q levels. Tyrobp knockout has been shown to decrease C1q accumulation, restoring long-term depression (LTD) and cognitive functions in neurodegenerative disease models, even in the presence of significant amyloid and tau pathology [85,86,89,96]. Our GENIE3 machine learning analysis identified a conserved regulatory network in EP and TG models, in which Tyrobp regulates Trem2, which in turn regulates C1q via C1qa (**Fig. 4E**). This regulatory hierarchy aligns with previous findings, suggesting a shared mechanism across EP and AD. Furthermore, correlations between these genes and changes in neuronal and microglial composition support the role of synaptic pruning in both conditions (**Fig. 5C**). The preservation of this pathway suggests that C1q-mediated synaptic dysfunction, which contributes to electrophysiological abnormalities in AD, may also be a mechanistic link between AD and EP.

In EP, complement system hyperactivation may lead to excessive synaptic pruning, disrupting the excitatory/inhibitory (E/I) balance, increasing neuronal hyperexcitability, and promoting seizures [97,98]. Status epilepticus, for instance, triggers prolonged activation of complement proteins—particularly C1q and C3—in the hippocampus, correlating with seizure frequency and severity [99]. In traumatic brain injury models, elevated C1q expression is associated with neuronal loss and epileptic spikes [100]. Blocking C1q or C3 in these models has been shown to reduce seizure frequency and severity [100]. Therefore, it was proposed that persistent activation of complement-mediated synaptic elimination may exacerbate disease by contributing to synaptic loss and network instability [94,97,98]. Excessive synaptic pruning may disproportionately target inhibitory synapses, which tilts the E/I balance toward excitation and promotes seizures [97,101,102].

In summary, the accumulation of amyloid plaques and tau tangles in AD activates microglia into a DAM state, marked by elevated expression of genes like Tyrobp and Trem2 involved in phagocytosis and inflammation. Tyrobp and Trem2 detect neuronal damage and recruit microglia for debris clearance and synaptic pruning via complement proteins like C1q. Normally, this helps to reduce plaque burden and maintain neural circuit integrity, but excessive pruning may disrupt the E/I balance, leading to hyperexcitability and seizures.

A limitation of our study is the reliance on animal models. Future research should prioritize clinical validation with large, well-characterized cohorts of AD patients with EP to bridge the gap between animal studies and potential therapeutic applications in humans.

## 5. Conclusions

This study provides a molecular framework for understanding the comorbidity between AD and EP by identifying shared molecular pathways and cellular mechanisms. Through comprehensive analysis of transcriptomic data from AD and EP mouse models and human patients, we identified a conserved set of DEGs and co-expression modules that implicate common pathological pathways in both conditions. Notably, the turquoise immune module was highly conserved across both disease models. Its shared hub genes, central to synaptic pruning, suggest that aberrant synaptic pruning may contribute to AD-related neurodegeneration and the hyperexcitability observed in EP. Future studies examining the regulatory roles of these hub genes in human patients may yield deeper insights into the complex interplay between neurodegeneration and epileptogenesis.

**Figures and legends**

**Figure 1: Differential Expression and Functional Enrichment Analyses in EP and AD Datasets**

**(A)** Volcano plot illustrating the DEGs in the EP dataset. The x-axis represents the log2 fold change, and the y-axis shows the -log10 adjusted p-value. Upregulated genes are highlighted in red, and downregulated genes are in blue. The dashed lines mark the thresholds for significance (adjusted p-value < 0.05 and |log2 fold change| > 1).

**(B)** Differential expression analysis of the TG dataset. Scatter plot showing progressive DEGs identified across different ages (4, 6, and 8 months) compared to their control and initial months. DEGs are color-coded based on their expression level (log2 fold change) compared to the control and initial month, with dot size to show significance (adjusted p-value). The shaded regions correspond to the different age groups, with the numbers indicating the count of EP-DEGs (numerator) and total DEGs (denominator) with a log2 fold change below 1 that marks the threshold for non-significant genes.

**(C)** The single upregulated progressive DEG, Cst7, detected in the J20 dataset across different ages (6, 8, 10, and 12 months). The plot shows the expression level of Cst7 over time (x-axis: Age in months; y-axis: Normalized counts), with different genotypes (J20 and WT) represented by different colors. Dashed lines represent mean paths for each age. (LRTstatistic=43.70, log2foldchange[6-12months] = 2.73, FDR=2.91E-5).

**(D)** KEGG pathway enrichment analysis of shared DEGs between the EP and TG datasets. The bubble plot indicates the significantly enriched pathways, with bubble size representing the gene count and color indicating the significance level (-log10 adjusted p-value).

**(E)** GO enrichment analysis of shared DEGs between the EP and TG datasets. The dot plot shows the enriched biological processes, molecular functions, and cellular components. Dot size corresponds to gene count, while color represents the

significance level (-log10 adjusted p-value). Key immune-related functions were prominently enriched.

**Figure 2: Co-Expression Network Construction and Model-Trait Association**

**(A-C)** Hierarchical clustering dendrograms are presented for the EP (A), TG (B), and J20 (C) datasets, with gene modules identified through dynamic tree cutting. The colors in the heatmap below each dendrogram correspond to distinct gene modules, where the clustering of similar colors between the EP and other datasets (TG and J20) reflects the conservation of modules across conditions. The GS is shown with darker colors indicating stronger correlations: red represents positive correlations, and blue represents negative correlations with disease genotypes (EP for panel A, TG for panel B, and J20 for panel C). Overlapping red areas in the module-trait relationships suggest that these modules may be positively correlated with both EP and AD, as seen in the turquoise module in the TG dataset. The DEG row shows the distribution of DEGs within the modules: red indicates DEGs, while grey indicates non-DEGs.

**(D-F)** Heatmaps of the module-trait relationships in EP (D), TG (E), and J20 (F) datasets. The heatmaps illustrate the Pearson correlation coefficients between MEs and genotypes. The color scale represents the strength and direction of the correlation, with red indicating positive and blue indicating negative correlations. Modules are considered as significant association with genotype using threshold (p-value $< 0.05$, $|r| > 0.65$).

**Figure 3: Module Preservation Analysis Across EP and AD Datasets**

**(A, D)** MedianRank preservation statistics of EP modules in the TG and J20 datasets, respectively. Each point represents an EP module, with its size indicating the module size and the color corresponding to the module color. The y-axis shows the median rank preservation statistic, with lower values indicating stronger preservation across the TG (A) and J20 (D) datasets.

**(B, E)** Zsummary preservation statistics of EP modules in the TG and J20 datasets, respectively. Each point represents an EP module, with the y-axis displaying the Zsummary preservation statistic. A Zsummary $> 10$ indicates strong evidence of preservation, $2 <$ Zsummary $< 10$ indicates moderate evidence, and Zsummary $< 5$ suggests no evidence of preservation. The gray horizontal line at Z=10 and the black horizontal line at Z=2 serve as reference points in the plots. The module size is indicated by the x-axis, and the color represents the module color.

**(C, F)** Cross-tabulation of EP modules with TG (C) and J20 (F) modules. The dot plots illustrate the overlap between EP modules (y-axis) and TG/J20 modules (x-axis). The color scale represents the adjusted p-value for the overlap significance, while the size of the dots corresponds to the number of overlapping genes. Larger, more significant dots indicate stronger overlaps between EP and AD modules, with particular emphasis on highly preserved modules like the turquoise module in the TG dataset. Only significantly overlapping with overlap count $> 30$ and adjusted p-value

< 0.05 was colored, while those with insignificant overlap are marked in gray.

**Figure 4: Identification and Network Analysis of Shared Hub Genes in EP and AD Datasets**

(**A**) Network plot illustrating the top 100 genes within the conserved turquoise module across both the EP and TG datasets. Each node represents a gene, and edges signify gene co-expression connections. Grey edges correspond to connections in the EP dataset, while blue edges represent those in the TG dataset. The color of the nodes indicates their level of connectivity, with deeper color signifying higher connectivity within the network such as Capg, Msn, and Npc2. Red nodes are shared hub genes that exhibit high connectivity in both networks and are DEGs under both conditions. Two shared hub genes not shown in the figure: Apobec and Cxcl16.

(**B**) Venn diagram depicting the overlap between hub genes identified in the EP and AD datasets and shared DEGs. 19 shared hub genes were identified as key drivers in both conditions.

(**C**) PPI network of the 19 shared hub genes, constructed using the STRING database. Nodes represent genes, and edges denote interactions, with highly connected genes such as C1qa, C1qb, and C1qc highlighted.

(**D**) Top 5 GO biological process enrichment terms based on p-values for the 19 shared hub genes, indicating their involvement in critical processes like synaptic pruning and complement system activation. The Sankey diagram on the left illustrates the distribution of genes across different GO terms, with the corresponding p-values on the right.

(**E**) Shared gene regulatory network inferred using the GENIE3 algorithm, showing the regulatory relationships among the shared hub genes. The network highlights a key regulatory pathway involving Tyrobp, Trem2, and C1q components genes, suggesting a common mechanism underlying immune responses and synaptic pruning in both EP and AD conditions.

(**F**) Progressive upregulation of key 5 shared hub genes involved in microglial synaptic pruning across different ages in the TG mouse model. The plot shows the expression level of these genes over time (x-axis: Age in months; y-axis: Normalized counts), with different genotypes represented by different colors (WT: black, TG: teal). Dashed lines represent mean paths for each age. LRT statistics of these genes can be found in **Table S2**.

**Figure 5: Cellular Composition Deconvolution and Association with Shared Hub Genes in EP and TG Datasets**

(**A**) Violin plots depicting the estimated proportions of different cell types (astrocytes, neurons, oligodendrocytes, microglia, and endothelial) in control and EP conditions. The x-axis represents different conditions, and the y-axis shows the proportions of specific cell types in each condition. A significant decrease in neuronal composition and an increase in microglial composition were observed in EP compared to control.

Asterisks significance statistical significance. The Mann-Whitney test was performed to determine significant cell composition ($P < 0.05$).

(**B**) Violin plots showing the estimated proportions of various cell types across control, EP, and TG conditions. The TG condition exhibited similar trends to EP, with a significant reduction in neuronal composition and an increase in microglial composition. The x-axis represents different conditions and time points, including Control (e.g., Control6, Control8) and experimental conditions (e.g., TG 6, TG 8). The y-axis shows the proportions of specific cell types (e.g., astrocytes, microglia, neurons) in each condition. Differences across conditions were statistically significant for most cell types, as indicated by the asterisks. The Kruskal-Wallis test was performed to determine the significance with the BH method was used to adjust the P-value in pairwise comparisons among different groups, with a significance level of $q < 0.05$.

(**C**) Heatmaps of Pearson correlation coefficients between the 19 shared hub genes and cell type compositions in EP (left) and TG (right) conditions. The correlation strength is color-coded, with blue indicating negative correlations and red indicating positive correlations. Strong negative correlations were found between shared hub genes (e.g., Tyrobp, Trem2, and C1q components) and neuronal composition, while positive correlations were observed with microglial and endothelial compositions, suggesting a potential role of these genes in immune response and inflammation. X marks denote low correlations ($r < 0.6$).

**Figure 6: Single-cell and Single-nucleus RNA Sequencing Analysis of Hub Gene Expression in Immune Cells of Epilepsy and Alzheimer's Disease Patients**

(**A, D**) Dot plot displaying the expression of shared hub genes across different identified cell types in the EP patient dataset. The size of the dots represents the proportion of cells expressing each gene, and the color intensity indicates the average expression level. (A) EP dataset, (D) AD dataset.

(**B, E**) t-SNE plot showing the clustering of cells in the EP and AD dataset based on their gene expression profiles, with distinct colors representing different cell types. (B) EP dataset, (E) AD dataset.

(**C, F**) Feature plots showing the expression patterns of individual hub genes within the EP dataset, over on the t-SNE map. Darker purple areas represent higher expression levels. TYROBP, TREM2, C1QA, C1QB, and C1QC exhibit high expression predominantly in microglia clusters. (C) EP dataset, (F) AD dataset.

**Legends of supplementary files**

**Table S1: Summary of Quality Control and Mapping Statistics for Bulk RNA-seq Samples**

Table S1 presents a detailed summary of the QC and mapping statistics for all RNA-seq samples analyzed in this study. For each sample, the total number of raw

reads, the number of reads passing quality filtering through Fastp, and the reads retained after rRNA contamination removal by ribodetector are reported. Additionally, the table includes the total number of reads aligned to the GRCm39.111 reference mouse genome and the percentage of reads successfully assigned to genomic features via featureCounts. Each sample is categorized by the experimental group, including relevant age and condition tags, and further classified into either the AD or EP dataset. Notes regarding any specific issues or annotations on individual samples are also provided.

**Table S2: Differential Expression and Functional Enrichment Analysis of Shared DEGs**

Table S2 presents a summary of differential expression and functional enrichment analyses across three datasets: EP, TG, and J20 mouse models. The DESeq2 analysis of the EP dataset identified 17,214 genes with varying expression levels and fold changes. For the TG dataset, the table provides FDR-adjusted p-values from a likelihood ratio test and fold changes at 4, 6, and 8 months of age, along with LRT statistics and corresponding p-values for 2,051 genes, while the J20 dataset highlighted Cst7 as the only significantly upregulated gene. Functional enrichment analysis of shared DEGs in EP and TG datasets revealed key biological processes, including immune and defense responses, that were shared between the EP and TG datasets.

**Table S3: Module Construction, Preservation, and Functional Enrichment of Gene Co-Expression Networks in Mouse Models**

Table S3 provides a summary of WGCNA on EP, TG, and J20 mouse models. The table is divided into multiple sections, including the gene modules' membership identified in each dataset and their correlations with model-specific genotypes. Additionally, module preservation analyses between the EP and AD datasets are included. GO enrichment analyses of the turquoise modules are also shown.

**Table S4: Protein-Protein Interaction Network and GO Biological Process Enrichment Analysis of Shared Hub Genes.**

Table S4 provides detailed analysis results of the PPI network constructed for 19 shared hub genes identified across EP and TG models. The table is divided into three sections. The PPI GO sheet summarizes the results of the GO biological process enrichment analysis. The PPI Degree sheet lists each gene and its degree of connectivity within the network. The PPI Interaction sheet details the specific interactions between these genes.

**Table S5: Regulatory Network Prediction Using GENIE3 for Turquoise Module in Mice Models**

Table S5 summarizes the results of regulatory network inference conducted using the

GENIE3 machine learning algorithm on the gene expression profiles of the turquoise module from the EP) and TG models. The table is divided into two sections: GENIE3TG and GENIE3EP, representing the predicted regulatory relationships within the TG and EP datasets, respectively. Each section lists the regulatory gene, the target gene, and the corresponding weight of the predicted regulatory interaction.

**Table S6: Cell Composition Deconvolution of Bulk RNA-seq Data**

Table S6 presents the results of cell composition deconvolution analysis conducted using CIBERSORT from BrainDeconvShiny on bulk RNA-seq data from the EP and AD models. The table includes the estimated proportions of major brain cell types, including neurons, astrocytes, oligodendrocytes, microglia, and endothelial for each sample, alongside the sample identifiers, group classification, age, and condition type (e.g., rTg4510, Wild Type).

**Figure S1. PCA of the EP dataset with outliers highlighted.**

Duplicate and low-quality samples were removed before analysis, and the variance-stabilizing transformation was applied to the count matrix. PCA was performed to explore potential outliers, and Mahalanobis distances were calculated based on the PCA scores. A chi-squared distribution threshold of 0.975 was used to identify significant outliers. A total of 11 outliers were detected and highlighted in red with their corresponding sample labels. These outliers were excluded from subsequent analyses.

**Figure S2. Hierarchical clustering dendrograms and trait heatmaps for the EP, rTg4510, and J20 datasets**.

(**A**) EP dataset, (**B**) rTg4510 dataset, and (**C)** J20 dataset. Hierarchical clustering was performed on variance-stabilized gene expression data to identify potential outliers. The top 85% of genes with the highest Median Absolute Deviation (MAD) were retained, and outliers were detected and removed before network construction. Two samples were removed from the rTg4510 dataset, and three samples were removed from the J20 dataset. The heatmaps below each dendrogram display the trait data associated with each sample, with red indicating outliers or specific traits of interest.

**Figure S3: Soft-thresholding power Selection and Comparability Assessment**

**(A)** Selection of the soft-thresholding power for network construction. The left panel shows the scale-free topology fit index (y-axis) as a function of the soft-thresholding power (x-axis) for EP, TG, and J20 datasets. The right panel depicts the mean connectivity (y-axis) against soft-thresholding power, indicating that a power of 9 was chosen for all datasets to achieve scale-free topology with $R^2 > 0.85$.

**(B)** Comparability assessment of the EP, TG, and J20 datasets. Scatter plots display the correlations between ranked mean gene expression (top) and ranked gene connectivity (bottom) between EP and TG datasets (left) and between EP and J20

datasets (right). Positive correlations and significant P values suggest strong comparability between datasets.

**Figure S4. Preservation and comparability of co-expression modules across EP, AD patient, and mouse model datasets.**

(**A**) Scale independence and mean connectivity plots across soft-thresholding powers for the EP (GSE63808) and AD (GSE132903) patient datasets, with a selected soft-thresholding power of 9 ensuring a scale-free topology ($R^2 \geq 0.85$).

(**B-C**) Dendrogram of gene modules identified in the EP and AD dataset using hierarchical clustering and dynamic tree cutting based on topological overlap matrices (TOM).

(**D-E**) Bubble plots show the overlap of modules between EP and EP mouse (EPM) models (D) and AD and TG mouse models (E). The turquoise module in both EP and TG models exhibits the highest preservation and overlap, suggesting a conserved molecular signature between species and disease states. The size of the bubbles represents the number of overlapping genes, and the color gradient reflects the p-values. Only significantly overlapping with overlap count > 30 and adjusted p-value < 0.05 was colored, while those with insignificant overlap are marked in gray. The turquoise modules also show significant positive correlations with disease genotype and contain the majority of DEGs in both models, underscoring their potential role in the shared molecular pathways of EP and AD.

**Figure S5. Progressive upregulation of shared hub genes across different ages in the TG mouse model.**

Gene expression profiles of remaining shared hub genes are shown across 4 time points: 2, 4, 6, and 8 months. The x-axis represents age in months, while the y-axis shows normalized expression counts. TG and WT genotypes are depicted by different colors (WT: black, TG: teal), with dashed lines representing mean paths for each age. LRT statistics of these genes can be found in **Table S2**.

**Figure S6: Cellular Composition Deconvolution and Association with Shared Hub Genes in J20 Datasets**

(**A**) Violin plots showing the estimated proportions of various cell types across control and J20 conditions at ages (6, 8, 10, and 12 months). The x-axis represents different conditions and time points, including Control (e.g., Control6, Control8) and experimental conditions (e.g., J20 6, J20 8). The y-axis shows the proportions of specific cell types (e.g., astrocytes, microglia, neurons) in each condition. No significant changes in cellular composition were observed across conditions in the J20 model. Differences across conditions were assessed using the Kruskal-Wallis test with the BH method for P-value adjustment in pairwise comparisons, no statistically significant differences ($q < 0.05$) were detected in this dataset.

(**B**) Heatmap of Pearson correlation coefficients between the 19 shared hub genes and

cell type compositions in the J20 dataset. The correlation strength is color-coded, with blue indicating negative correlations and red indicating positive correlations. Strong positive correlations were observed between hub genes such as Tyrobp, Trem2, and complement system components (C1qa, C1qb, C1qc) and microglial composition, suggesting their specific expression in microglia. No bubble is displayed on the heatmap, which means it is statistically insignificant.

**Figure S7: Expression Localization of Shared Hub Genes in Mouse Brain Cell Types Using the Whole Mouse Brain Transcriptomic Cell Type Atlas**

This figure shows the expression patterns of 19 shared hub genes across various cell types in the mouse brain, based on the Whole Mouse Brain Transcriptomic Cell Type Atlas (https://assets.nemoarchive.org/dat-qg7n1b0) from the Allen Brain Cell Atlas (Yao, Zizhen, et al., 2023). The top left panel illustrates the localization and color of various cell types, such as astrocytes, microglia, macrophages, endothelial cells, and oligodendrocytes in the brain atlas. Each circular panel highlights the specific expression profile of one gene, with darker shading representing higher expression levels. Most of these genes (15 out of 19) are predominantly expressed in immune cells, specifically microglia and macrophages.

**Data and code availability**

All sequencing and microarray data used in this study are publicly accessible through the National Center for Biotechnology Information (NCBI) under the following accession numbers: PRJEB18790, GSE125957, GSE63808, GSE132903, GSE201048, and GSE227223. The code supporting the analyses, along with the normalized gene expression matrix, is available at https://github.com/HuihongLi/AD-EP-MS-Code. Additional data can be provided upon reasonable request to the corresponding authors.

**CRediT authorship contribution statement**

Huihong Li: Conceptualization, Investigation, Methodology, Writing – original draft, Writing – review & editing, Formal analysis.
Jianwei Li: Writing – original draft, Writing – review & editing
Mingjie Chen: Investigation, Writing – review & editing
Xueke Liu: Investigation, Writing – review & editing
Yushan Sun: Investigation, Writing – review & editing
Jie Wu: Conceptualization, Supervision, Writing – original, Writing – review & editing
Bingying Lin: Investigation
Si Chen: Writing – review & editing
Zihan Deng: Writing – review & editing
Mengqi Hong: Writing – review & editing

Nai-Li Wei: Conceptualization, Writing – original draft, Writing – review & editing
Xiaoyu Ji: Conceptualization, Supervision, Funding acquisition, Writing – original, Writing – review & editing

**Funding statement**
This research was supported by the Young Scientists Fund of the National Natural Science Foundation of China (Grant Nos. 82201629) and the Guangdong Provincial Science and Technology Special Fund (Grant Nos. 210803136872196)

**Declaration of Competing Interest**
The authors declare that they have no known competing financial interests or personal relationships that could have appeared to influence the work reported in this paper.

**Acknowledgments**
We thank our lab members for engaging in discussions and improving the manuscript.

**References:**

1. Giorgi, F. S., Saccaro, L. F., Busceti, C. L., Biagioni, F. & Fornai, F. Epilepsy and Alzheimer's Disease: Potential mechanisms for an association. *Brain Research Bulletin* vol. 160 Preprint at https://doi.org/10.1016/j.brainresbull.2020.04.009 (2020).
2. Fang, Y. *et al*. Alzheimer Disease and Epilepsy: A Mendelian Randomization Study. *Neurology* **101**, (2023).
3. Kamondi, A., Grigg-Damberger, M., Löscher, W., Tanila, H. & Horvath, A. A. Epilepsy and epileptiform activity in late-onset Alzheimer disease: clinical and pathophysiological advances, gaps and conundrums. *Nature Reviews Neurology* vol. 20 Preprint at https://doi.org/10.1038/s41582-024-00932-4 (2024).
4. Wimo, A., Jönsson, L., Bond, J., Prince, M. & Winblad, B. The worldwide economic impact of dementia 2010. *Alzheimer's and Dementia* **9**, (2013).
5. Bloom, G. S. Amyloid-β and tau: The trigger and bullet in Alzheimer disease pathogenesis. *JAMA Neurol* **71**, (2014).
6. Liu, K. Y., Stringer, A. E., Reeves, S. J. & Howard, R. J. The neurochemistry of agitation in Alzheimer's disease: a systematic review. *Ageing Research Reviews* vol. 43 Preprint at https://doi.org/10.1016/j.arr.2018.03.003 (2018).
7. Ardura-Fabregat, A. *et al.* Targeting Neuroinflammation to Treat Alzheimer's Disease. *CNS Drugs* vol. 31 Preprint at https://doi.org/10.1007/s40263-017-0483-3 (2017).
8. Ngugi, A. K., Bottomley, C., Kleinschmidt, I., Sander, J. W. & Newton, C. R. Estimation of the burden of active and life-time epilepsy: A meta-analytic approach. *Epilepsia* **51**, (2010).
9. Mendez, M. F. & Lim, G. T. H. Seizures in elderly patients with dementia:

Epidemiology and management. *Drugs Aging* **20**, (2003).

10. Lehmann, L., Lo, A., Knox, K. M. & Barker-Haliski, M. Alzheimer's Disease and Epilepsy: A Perspective on the Opportunities for Overlapping Therapeutic Innovation. *Neurochemical Research* vol. 46 Preprint at https://doi.org/10.1007/s11064-021-03332-y (2021).
11. Ghosh, S. *et al.* Pharmacological and therapeutic approaches in the treatment of epilepsy. *Biomedicines* vol. 9 Preprint at https://doi.org/10.3390/biomedicines9050470 (2021).
12. Yiannopoulou, K. G. & Papageorgiou, S. G. Current and future treatments for Alzheimer's disease. *Therapeutic Advances in Neurological Disorders* vol. 6 Preprint at https://doi.org/10.1177/1756285612461679 (2013).
13. Leitner, D. *et al.* Similar brain proteomic signatures in Alzheimer's disease and epilepsy. *Acta Neuropathol* **147**, (2024).
14. Pandis, D. & Scarmeas, N. Seizures in Alzheimer Disease: Clinical and Epidemiological Data. *https://doi.org/10.5698/1535-7511-12.5.184* **12**, 184–187 (2012).
15. Xu, L. & Wang, Q. The bidirectional relationship between Alzheimer's disease (AD) and epilepsy: A Mendelian randomization study. *Brain Behav* **13**, (2023).
16. Tai, X. Y. *et al.* Hyperphosphorylated tau in patients with refractory epilepsy correlates with cognitive decline: A study of temporal lobe resections. *Brain* **139**, (2016).
17. Thom, M. *et al.* Neurofibrillary tangle pathology and Braak staging in chronic epilepsy in relation to traumatic brain injury and hippocampal sclerosis: A post-mortem study. *Brain* **134**, (2011).
18. Mackenzie, I. R. A. & Miller, L. A. Senile plaques in temporal lobe epilepsy. *Acta Neuropathol* **87**, (1994).
19. del Pozo, A. *et al.* Chronic evoked seizures in young pre-symptomatic APP/PS1 mice induce serotonin changes and accelerate onset of Alzheimer's disease-related neuropathology. *Prog Neurobiol* **235**, (2024).
20. Gureviciene, I. *et al.* Characterization of Epileptic Spiking Associated With Brain Amyloidosis in APP/PS1 Mice. *Front Neurol* **10**, (2019).
21. Vande Vyver, M. *et al.* Higher susceptibility to 6 Hz corneal kindling and lower responsiveness to antiseizure drugs in mouse models of Alzheimer's disease. *Epilepsia* **63**, (2022).
22. Lisgaras, C. P. & Scharfman, H. E. High-frequency oscillations (250–500 Hz) in animal models of Alzheimer's disease and two animal models of epilepsy. *Epilepsia* **64**, (2023).
23. Paudel, Y. N., Angelopoulou, E., Piperi, C., Othman, I. & Shaikh, M. F. Revisiting the impact of neurodegenerative proteins in epilepsy: Focus on alpha-synuclein, beta-amyloid, and Tau. *Biology* vol. 9 Preprint at https://doi.org/10.3390/biology9060122 (2020).
24. Hwang, K., Vaknalli, R. N., Addo-Osafo, K., Vicente, M. & Vossel, K.

Tauopathy and Epilepsy Comorbidities and Underlying Mechanisms. *Frontiers in Aging Neuroscience* vol. 14 Preprint at https://doi.org/10.3389/fnagi.2022.903973 (2022).

25. Toral-Rios, D., Pichardo-Rojas, P. S., Alonso-Vanegas, M. & Campos-Peña, V. GSK3β and Tau Protein in Alzheimer's Disease and Epilepsy. *Frontiers in Cellular Neuroscience* vol. 14 Preprint at https://doi.org/10.3389/fncel.2020.00019 (2020).
26. Larner, A. J. Presenilin-1 mutation Alzheimer's disease: A genetic epilepsy syndrome? *Epilepsy and Behavior* vol. 21 Preprint at https://doi.org/10.1016/j.yebeh.2011.03.022 (2011).
27. Jiang, X. *et al.* The overlap between Alzheimer's disease and epilepsy uncovered by transcriptome sequencing. *Clin Transl Med* **10**, (2020).
28. Jankovic, S. M. & Dostic, M. Choice of antiepileptic drugs for the elderly: Possible drug interactions and adverse effects. *Expert Opinion on Drug Metabolism and Toxicology* vol. 8 Preprint at https://doi.org/10.1517/17425255.2012.645535 (2012).
29. Bosco, F. *et al.* Antiseizure Medications in Alzheimer's Disease from Preclinical to Clinical Evidence. *International Journal of Molecular Sciences* vol. 24 Preprint at https://doi.org/10.3390/ijms241612639 (2023).
30. Hasin, Y., Seldin, M. & Lusis, A. Multi-omics approaches to disease. *Genome Biology* vol. 18 Preprint at https://doi.org/10.1186/s13059-017-1215-1 (2017).
31. Srivastava, P. K. *et al.* Genome-wide analysis of differential RNA editing in epilepsy. *Genome Res* **27**, (2017).
32. Castanho, I. *et al.* Transcriptional Signatures of Tau and Amyloid Neuropathology. *Cell Rep* **30**, (2020).
33. Johnson, M. R. *et al.* Systems genetics identifies Sestrin 3 as a regulator of a proconvulsant gene network in human epileptic hippocampus. *Nat Commun* **6**, (2015).
34. Piras, I. S. *et al.* Transcriptome Changes in the Alzheimer's Disease Middle Temporal Gyrus: Importance of RNA Metabolism and Mitochondria-Associated Membrane Genes. *Journal of Alzheimer's Disease* **70**, (2019).
35. Kumar, P. *et al.* Single-cell transcriptomics and surface epitope detection in human brain epileptic lesions identifies pro-inflammatory signaling. *Nat Neurosci* **25**, (2022).
36. Sun, N. *et al.* Human microglial state dynamics in Alzheimer's disease progression. *Cell* **186**, (2023).
37. Andrews, S. FastQC. *Babraham Bioinformatics* (2010).
38. Chen, S., Zhou, Y., Chen, Y. & Gu, J. Fastp: An ultra-fast all-in-one FASTQ preprocessor. in *Bioinformatics* vol. 34 (2018).
39. Deng, Z. L., Münch, P. C., Mreches, R. & McHardy, A. C. Rapid and accurate identification of ribosomal RNA sequences via deep learning. *Nucleic Acids*

*Res* **50**, (2022).
40. Kim, D., Paggi, J. M., Park, C., Bennett, C. & Salzberg, S. L. Graph-based genome alignment and genotyping with HISAT2 and HISAT-genotype. *Nat Biotechnol* **37**, (2019).
41. Liao, Y., Smyth, G. K. & Shi, W. FeatureCounts: An efficient general purpose program for assigning sequence reads to genomic features. *Bioinformatics* **30**, (2014).
42. Love, M. I., Huber, W. & Anders, S. Moderated estimation of fold change and dispersion for RNA-seq data with DESeq2. *Genome Biol* **15**, (2014).
43. Liao, Y., Wang, J., Jaehnig, E. J., Shi, Z. & Zhang, B. WebGestalt 2019: gene set analysis toolkit with revamped UIs and APIs. *Nucleic Acids Res* **47**, (2019).
44. Miller, J. A., Horvath, S. & Geschwind, D. H. Divergence of human and mouse brain transcriptome highlights Alzheimer disease pathways. *Proc Natl Acad Sci U S A* **107**, (2010).
45. Langfelder, P. & Horvath, S. WGCNA: An R package for weighted correlation network analysis. *BMC Bioinformatics* **9**, (2008).
46. Zhang, B. & Horvath, S. A general framework for weighted gene co-expression network analysis. *Stat Appl Genet Mol Biol* **4**, (2005).
47. Ritchie, M. E. *et al.* Limma powers differential expression analyses for RNA-sequencing and microarray studies. *Nucleic Acids Res* **43**, (2015).
48. Schober, P. & Schwarte, L. A. Correlation coefficients: Appropriate use and interpretation. *Anesth Analg* **126**, (2018).
49. Langfelder, P., Luo, R., Oldham, M. C. & Horvath, S. Is my network module preserved and reproducible? *PLoS Comput Biol* **7**, (2011).
50. Szklarczyk, D. *et al.* The STRING database in 2023: protein-protein association networks and functional enrichment analyses for any sequenced genome of interest. *Nucleic Acids Res* **51**, (2023).
51. Zhou, G. *et al.* NetworkAnalyst 3.0: A visual analytics platform for comprehensive gene expression profiling and meta-analysis. *Nucleic Acids Res* **47**, (2019).
52. Huynh-Thu, V. A., Irrthum, A., Wehenkel, L. & Geurts, P. Inferring regulatory networks from expression data using tree-based methods. *PLoS One* **5**, (2010).
53. Shannon, P. *et al.* Cytoscape: A software Environment for integrated models of biomolecular interaction networks. *Genome Res* **13**, (2003).
54. Newman, A. M. *et al.* Robust enumeration of cell subsets from tissue expression profiles. *Nat Methods* **12**, (2015).
55. Sutton, G. J. *et al.* Comprehensive evaluation of deconvolution methods for human brain gene expression. *Nat Commun* **13**, (2022).
56. Robinson, M. D., McCarthy, D. J. & Smyth, G. K. edgeR: A Bioconductor package for differential expression analysis of digital gene expression data. *Bioinformatics* **26**, (2009).
57. Zhang, Y. *et al.* An RNA-sequencing transcriptome and splicing database of

glia, neurons, and vascular cells of the cerebral cortex. *Journal of Neuroscience* **34**, (2014).

58. Hao, Y. *et al.* Dictionary learning for integrative, multimodal and scalable single-cell analysis. *Nat Biotechnol* **42**, (2024).
59. Yao, Z. *et al.* A high-resolution transcriptomic and spatial atlas of cell types in the whole mouse brain. *Nature* **624**, (2023).
60. Eng, L. F., Ghirnikar, R. S. & Lee, Y. L. Glial Fibrillary Acidic Protein: GFAP-Thirty-One Years (1969-2000). *Neurochem Res* **25**, (2000).
61. Jurga, A. M., Paleczna, M. & Kuter, K. Z. Overview of General and Discriminating Markers of Differential Microglia Phenotypes. *Front Cell Neurosci* **14**, (2020).
62. Pekny, M. & Pekna, M. Astrocyte reactivity and reactive astrogliosis: Costs and benefits. *Physiol Rev* **94**, (2014).
63. Streit, W. J., Mrak, R. E. & Griffin, W. S. T. Microglia and neuroinflammation: A pathological perspective. *J Neuroinflammation* **1**, (2004).
64. Chen, Z. P. *et al.* Lipid-accumulated reactive astrocytes promote disease progression in epilepsy. *Nat Neurosci* **26**, (2023).
65. Wyss-Coray, T. Inflammation in Alzheimer disease: Driving force, bystander or beneficial response? *Nature Medicine* vol. 12 Preprint at (2006).
66. Seifert, G., Carmignoto, G. & Steinhäuser, C. Astrocyte dysfunction in epilepsy. *Brain Research Reviews* vol. 63 Preprint at https://doi.org/10.1016/j.brainresrev.2009.10.004 (2010).
67. Onyango, I. G., Jauregui, G. V., Čarná, M., Bennett, J. P. & Stokin, G. B. Neuroinflammation in Alzheimer's disease. *Biomedicines* vol. 9 Preprint at https://doi.org/10.3390/biomedicines9050524 (2021).
68. Vezzani, A., French, J., Bartfai, T. & Baram, T. Z. The role of inflammation in epilepsy. *Nature Reviews Neurology 2010 7:1* **7**, 31–40 (2010).
69. Vezzani, A. & Viviani, B. Neuromodulatory properties of inflammatory cytokines and their impact on neuronal excitability. *Neuropharmacology* **96**, 70–82 (2015).
70. Heneka, M. T., Golenbock, D. T. & Latz, E. Innate immunity in Alzheimer's disease. *Nature Immunology 2015 16:3* **16**, 229–236 (2015).
71. van Vliet, E. A., Aronica, E. & Gorter, J. A. Blood-brain barrier dysfunction, seizures and epilepsy. *Seminars in Cell and Developmental Biology* vol. 38 Preprint at https://doi.org/10.1016/j.semcdb.2014.10.003 (2015).
72. Zlokovic, B. V. Neurovascular pathways to neurodegeneration in Alzheimer's disease and other disorders. *Nature Reviews Neuroscience* vol. 12 Preprint at https://doi.org/10.1038/nrn3114 (2011).
73. Kopczynska, M. *et al.* Complement system biomarkers in epilepsy. *Seizure* **60**, (2018).
74. Veerhuis, R., Nielsen, H. M. & Tenner, A. J. Complement in the brain. *Molecular Immunology* vol. 48 Preprint at

https://doi.org/10.1016/j.molimm.2011.04.003 (2011).

75. Zhong, L. *et al.* TREM2 receptor protects against complement-mediated synaptic loss by binding to complement C1q during neurodegeneration. *Immunity* **56**, (2023).

76. Hong, S. *et al.* Complement and microglia mediate early synapse loss in Alzheimer mouse models. *Science (1979)* **352**, (2016).

77. Aronica, E. *et al.* Complement activation in experimental and human temporal lobe epilepsy. *Neurobiol Dis* **26**, (2007).

78. Liew, Y. *et al.* Neuroinflammation: A Common Pathway in Alzheimer's Disease and Epilepsy. *Journal of Alzheimer's Disease* vol. 94 Preprint at https://doi.org/10.3233/JAD-230059 (2023).

79. Vossel, K. A. *et al.* Seizures and epileptiform activity in the early stages of Alzheimer disease. *JAMA Neurol* **70**, (2013).

80. Gourmaud, S. *et al.* Alzheimer-like amyloid and tau alterations associated with cognitive deficit in temporal lobe epilepsy. *Brain* **143**, (2020).

81. Youssef, F. S., Menze, E. T. & Ashour, M. L. A potent lignan from prunes alleviates inflammation and oxidative stress in lithium/pilocarpine-induced epileptic seizures in rats. *Antioxidants* **9**, (2020).

82. Paolicelli, R. C. & Ferretti, M. T. Function and dysfunction of microglia during brain development: Consequences for synapses and neural circuits. *Frontiers in Synaptic Neuroscience* vol. 9 Preprint at https://doi.org/10.3389/fnsyn.2017.00009 (2017).

83. Stevens, B. *et al.* The Classical Complement Cascade Mediates CNS Synapse Elimination. *Cell* **131**, (2007).

84. Filipello, F. *et al.* The Microglial Innate Immune Receptor TREM2 Is Required for Synapse Elimination and Normal Brain Connectivity. *Immunity* **48**, (2018).

85. Haure-Mirande, J. V., Audrain, M., Ehrlich, M. E. & Gandy, S. Microglial TYROBP/DAP12 in Alzheimer's disease: Transduction of physiological and pathological signals across TREM2. *Molecular Neurodegeneration* vol. 17 Preprint at https://doi.org/10.1186/s13024-022-00552-w (2022).

86. Haure-Mirande, J. V. *et al.* Deficiency of TYROBP, an adapter protein for TREM2 and CR3 receptors, is neuroprotective in a mouse model of early Alzheimer's pathology. *Acta Neuropathol* **134**, 769–788 (2017).

87. Hou, J., Chen, Y., Grajales-Reyes, G. & Colonna, M. TREM2 dependent and independent functions of microglia in Alzheimer's disease. *Molecular Neurodegeneration 2022 17:1* **17**, 1–19 (2022).

88. Ma, J., Jiang, T., Tan, L. & Yu, J. T. TYROBP in Alzheimer's Disease. *Mol Neurobiol* **51**, 820–826 (2015).

89. Audrain, M. *et al.* Integrative approach to sporadic Alzheimer's disease: deficiency of TYROBP in a tauopathy mouse model reduces C1q and normalizes clinical phenotype while increasing spread and state of phosphorylation of tau. *Mol Psychiatry* **24**, (2019).

90. Carvalho, K. *et al.* Exacerbation of C1q dysregulation, synaptic loss and memory deficits in tau pathology linked to neuronal adenosine A2A receptor. *Brain* **142**, (2019).
91. Dejanovic, B. *et al.* Complement C1q-dependent excitatory and inhibitory synapse elimination by astrocytes and microglia in Alzheimer's disease mouse models. *Nat Aging* **2**, (2022).
92. Dejanovic, B. *et al.* Changes in the Synaptic Proteome in Tauopathy and Rescue of Tau-Induced Synapse Loss by C1q Antibodies. *Neuron* **100**, (2018).
93. Stephan, A. H. *et al.* A dramatic increase of C1q protein in the CNS during normal aging. *Journal of Neuroscience* **33**, (2013).
94. Wu, X. *et al.* Complement C1q drives microglia-dependent synaptic loss and cognitive impairments in a mouse model of lipopolysaccharide-induced neuroinflammation. *Neuropharmacology* **237**, (2023).
95. Gomez-Arboledas, A. *et al.* C5aR1 signaling promotes region- and age-dependent synaptic pruning in models of Alzheimer's disease. *Alzheimer's and Dementia* **20**, (2024).
96. Audrain, M. *et al.* Integrative approach to sporadic Alzheimer's disease: deficiency of TYROBP in a tauopathy mouse model reduces C1q and normalizes clinical phenotype while increasing spread and state of phosphorylation of tau. *Molecular Psychiatry 2018 24:9* **24**, 1383–1397 (2018).
97. Andoh, M., Ikegaya, Y. & Koyama, R. Synaptic pruning by microglia in epilepsy. *Journal of Clinical Medicine* vol. 8 Preprint at https://doi.org/10.3390/jcm8122170 (2019).
98. Wyatt, S. K., Witt, T., Barbaro, N. M., Cohen-Gadol, A. A. & Brewster, A. L. Enhanced classical complement pathway activation and altered phagocytosis signaling molecules in human epilepsy. *Exp Neurol* **295**, (2017).
99. Schartz, N. D., Wyatt-Johnson, S. K., Price, L. R., Colin, S. A. & Brewster, A. L. Status epilepticus triggers long-lasting activation of complement C1q-C3 signaling in the hippocampus that correlates with seizure frequency in experimental epilepsy. *Neurobiol Dis* **109**, (2018).
100. Holden, S. S. *et al.* Complement factor C1q mediates sleep spindle loss and epileptic spikes after mild brain injury. *Science (1979)* **373**, (2021).
101. Ferecskó, A. S. *et al.* Structural and functional substrates of tetanus toxin in an animal model of temporal lobe epilepsy. *Brain Struct Funct* **220**, 1013 (2015).
102. Lui, H. *et al.* Progranulin Deficiency Promotes Circuit-Specific Synaptic Pruning by Microglia via Complement Activation. *Cell* **165**, (2016).

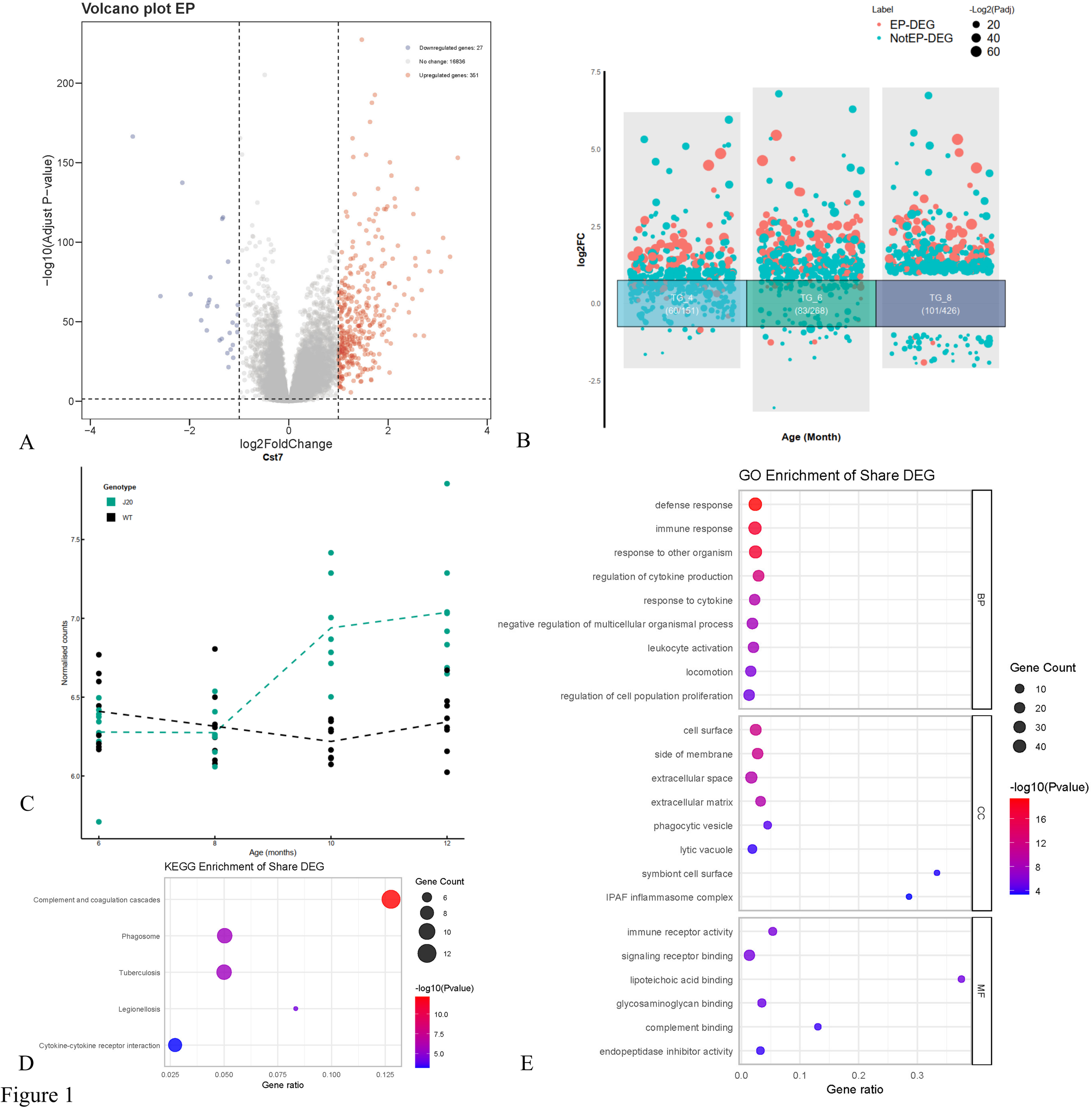
Volcano plot EP
Downregulated genes: 27
No change: 16836
Upregulated genes: 351
−log10(Adjust P−value)
log2FoldChange
A
Label
EP-DEG
NotEP-DEG
-Log2(Padj)
20
40
60
log2FC
TG_4
(60/151)
TG_6
(83/268)
TG_8
(101/426)
Age (Month)
B
Cst7
Genotype
J20
WT
Normalised counts
Age (months)
C
KEGG Enrichment of Share DEG
Complement and coagulation cascades
Phagosome
Tuberculosis
Legionellosis
Cytokine-cytokine receptor interaction
Gene ratio
Gene Count
-log10(Pvalue)
D
GO Enrichment of Share DEG
defense response
immune response
response to other organism
regulation of cytokine production
response to cytokine
negative regulation of multicellular organismal process
leukocyte activation
locomotion
regulation of cell population proliferation
BP
cell surface
side of membrane
extracellular space
extracellular matrix
phagocytic vesicle
lytic vacuole
symbiont cell surface
IPAF inflammasome complex
CC
immune receptor activity
signaling receptor binding
lipoteichoic acid binding
glycosaminoglycan binding
complement binding
endopeptidase inhibitor activity
MF
Gene ratio
Gene Count
-log10(Pvalue)
E

Figure 1

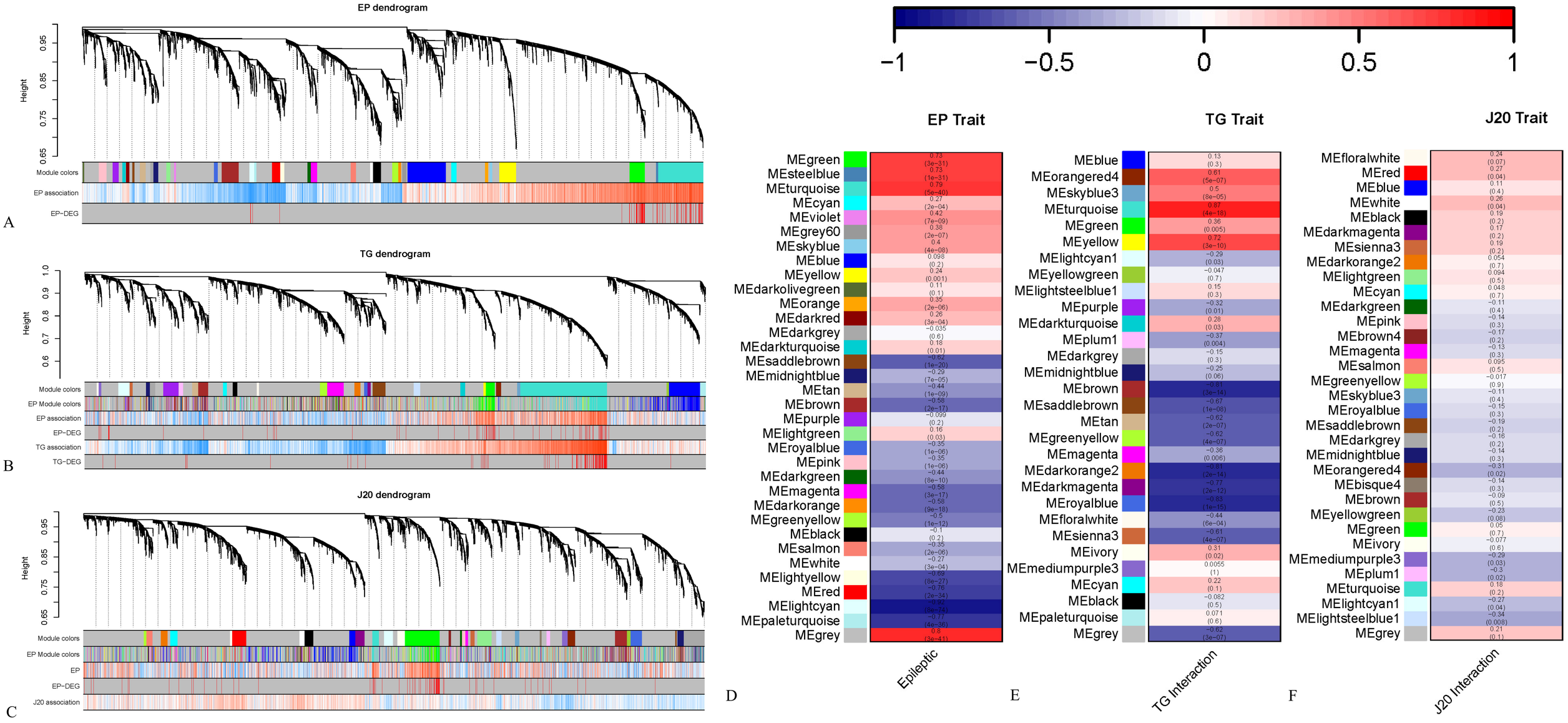
EP dendrogram
Height
Module colors
EP association
EP-DEG
A
TG dendrogram
Module colors
EP Module colors
EP association
EP-DEG
TG association
TG-DEG
B
J20 dendrogram
Module colors
EP Module colors
EP
EP-DEG
J20 association
C
−1
−0.5
0
0.5
1
EP Trait
MEgreen 0.73 (3e−31)
MEsteelblue 0.73 (1e−31)
MEturquoise 0.79 (5e−40)
MEcyan 0.27 (2e−04)
MEviolet 0.42 (7e−09)
MEgrey60 0.38 (2e−07)
MEskyblue 0.4 (4e−08)
MEblue 0.098 (0.2)
MEyellow 0.24 (0.001)
MEdarkolivegreen 0.11 (0.1)
MEorange 0.35 (2e−06)
MEdarkred 0.26 (3e−04)
MEdarkgrey −0.035 (0.6)
MEdarkturquoise 0.18 (0.01)
MEsaddlebrown −0.52 (1e−20)
MEmidnightblue −0.29 (7e−05)
MEtan −0.44 (1e−09)
MEbrown −0.58 (2e−17)
MEpurple −0.099 (0.2)
MElightgreen 0.16 (0.03)
MEroyalblue −0.35 (1e−06)
MEpink −0.35 (1e−06)
MEdarkgreen −0.44 (8e−10)
MEmagenta −0.58 (3e−17)
MEdarkorange −0.58 (9e−18)
MEgreenyellow −0.5 (1e−12)
MEblack −0.1 (0.2)
MEsalmon −0.35 (2e−06)
MEwhite −0.27 (3e−04)
MElightyellow −0.69 (8e−27)
MEred −0.76 (2e−34)
MElightcyan −0.92 (8e−74)
MEpaleturquoise −0.77 (4e−36)
MEgrey 0.8 (3e−41)
Epileptic
D
TG Trait
MEblue 0.13 (0.3)
MEorangered4 0.61 (5e−07)
MEskyblue3 0.5 (8e−05)
MEturquoise 0.87 (4e−18)
MEgreen 0.36 (0.005)
MEyellow 0.72 (3e−10)
MElightcyan1 −0.29 (0.03)
MEyellowgreen −0.047 (0.7)
MElightsteelblue1 0.15 (0.3)
MEpurple −0.32 (0.01)
MEdarkturquoise 0.28 (0.03)
MEplum1 −0.37 (0.004)
MEdarkgrey −0.15 (0.3)
MEmidnightblue −0.25 (0.06)
MEbrown −0.81 (3e−14)
MEsaddlebrown −0.67 (1e−08)
MEtan −0.62 (2e−07)
MEgreenyellow −0.62 (4e−07)
MEmagenta −0.36 (0.006)
MEdarkorange2 −0.81 (2e−14)
MEdarkmagenta −0.77 (2e−12)
MEroyalblue −0.83 (1e−15)
MEfloralwhite −0.44 (6e−04)
MEsienna3 −0.61 (4e−07)
MEivory 0.31 (0.02)
MEmediumpurple3 0.0055 (1)
MEcyan 0.22 (0.1)
MEblack −0.082 (0.5)
MEpaleturquoise 0.071 (0.6)
MEgrey −0.62 (3e−07)
TG Interaction
E
J20 Trait
MEfloralwhite 0.24 (0.07)
MEred 0.27 (0.04)
MEblue 0.11 (0.4)
MEwhite 0.26 (0.04)
MEblack 0.19 (0.2)
MEdarkmagenta 0.17 (0.2)
MEsienna3 0.19 (0.2)
MEdarkorange2 0.054 (0.7)
MElightgreen 0.094 (0.5)
MEcyan 0.048 (0.7)
MEdarkgreen −0.11 (0.4)
MEpink −0.14 (0.3)
MEbrown4 −0.17 (0.2)
MEmagenta −0.13 (0.3)
MEsalmon 0.095 (0.5)
MEgreenyellow −0.017 (0.9)
MEskyblue3 −0.11 (0.4)
MEroyalblue −0.15 (0.3)
MEsaddlebrown −0.19 (0.2)
MEdarkgrey −0.16 (0.2)
MEmidnightblue −0.14 (0.3)
MEorangered4 −0.31 (0.02)
MEbisque4 −0.14 (0.3)
MEbrown −0.09 (0.5)
MEyellowgreen −0.23 (0.08)
MEgreen 0.05 (0.7)
MEivory −0.077 (0.6)
MEmediumpurple3 −0.29 (0.03)
MEplum1 −0.3 (0.02)
MEturquoise 0.18 (0.2)
MElightcyan1 −0.27 (0.04)
MElightsteelblue1 −0.34 (0.008)
MEgrey 0.21 (0.1)
J20 Interaction
F

Figure 2

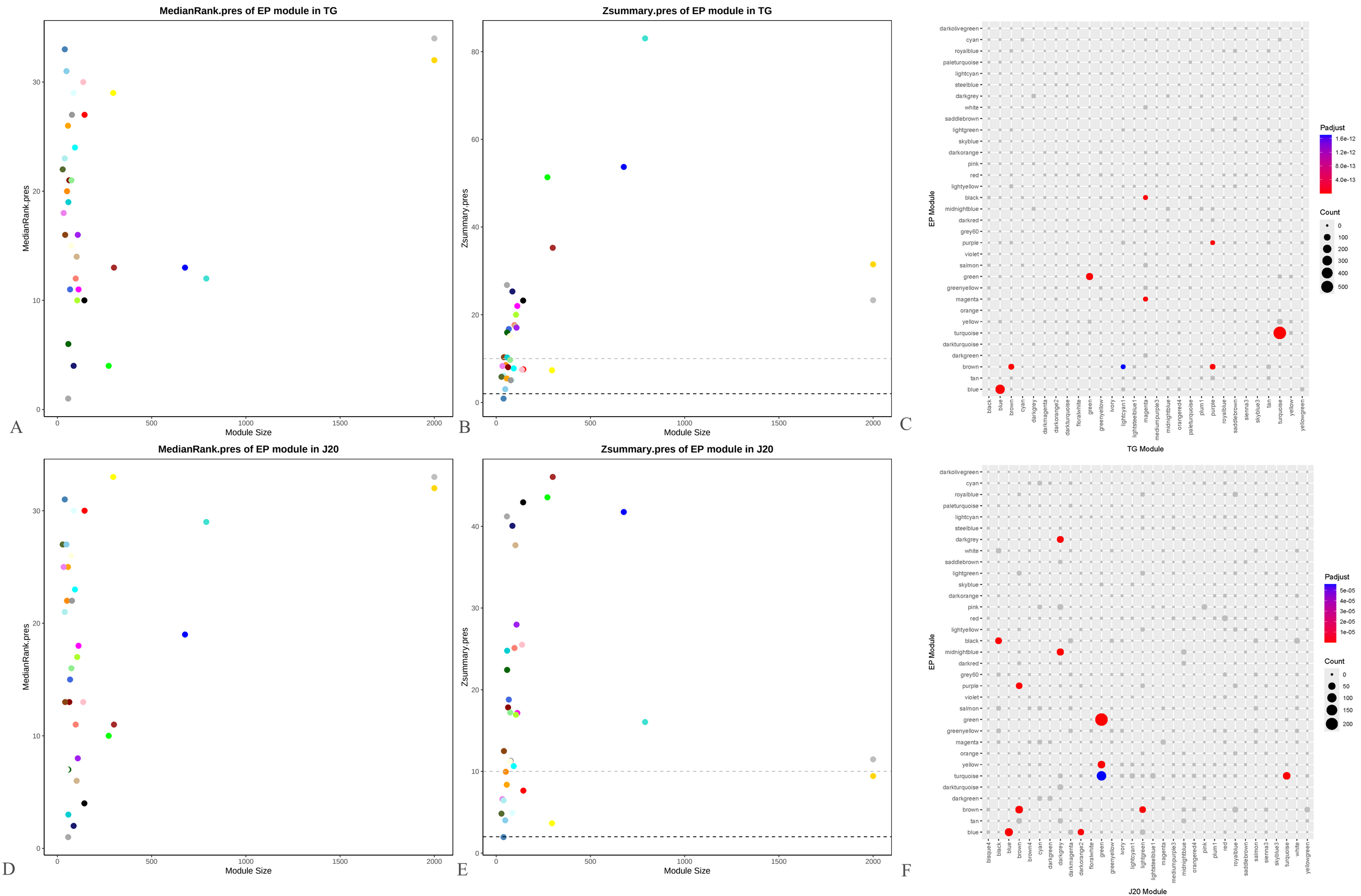
MedianRank.pres of EP module in TG
Zsummary.pres of EP module in TG
MedianRank.pres of EP module in J20
Zsummary.pres of EP module in J20
MedianRank.pres
Zsummary.pres
Module Size
EP Module
TG Module
J20 Module
Padjust
Count
A
B
C
D
E
F

Figure 3

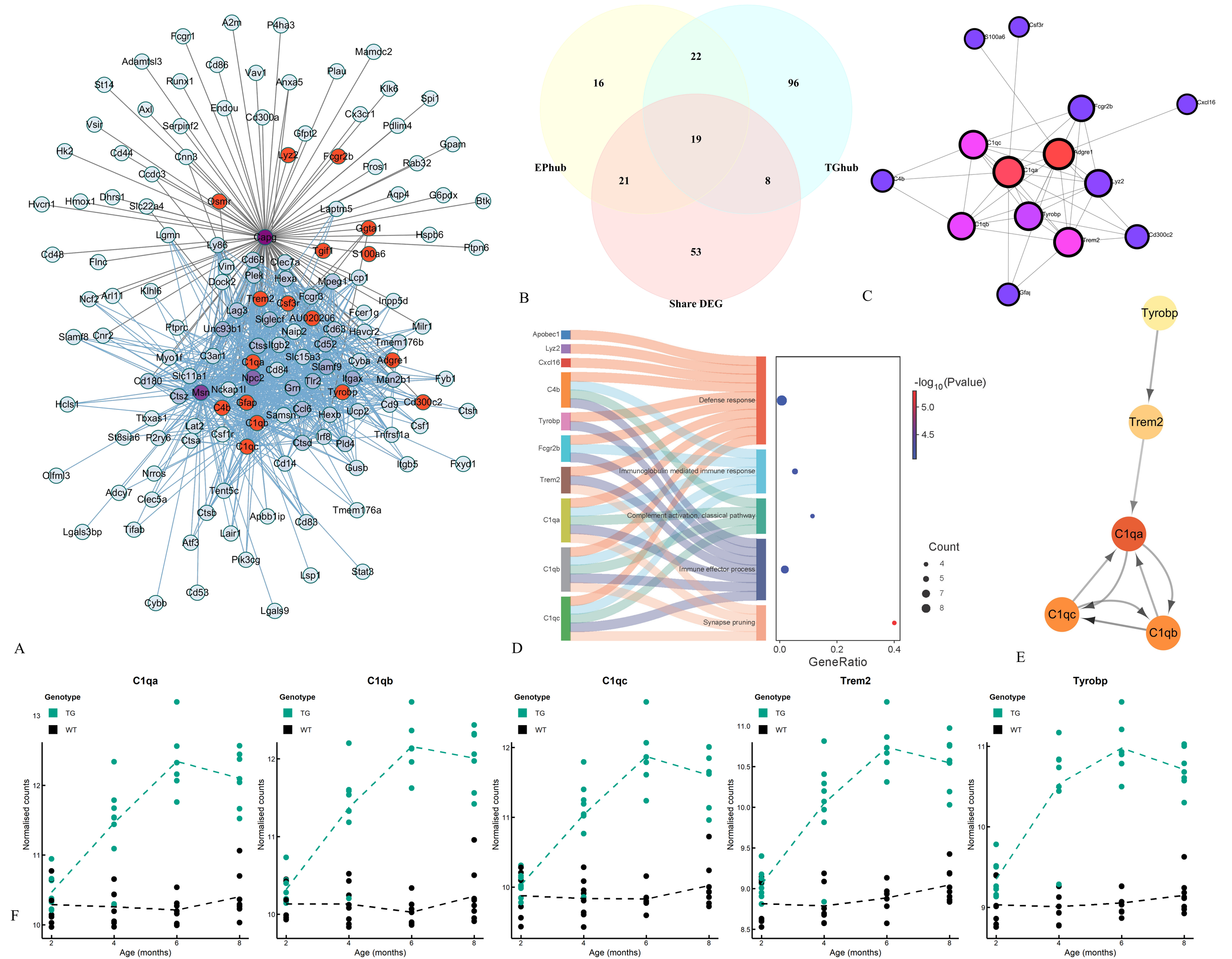
A
B
EPhub
TGhub
Share DEG
16
22
96
19
21
8
53
C
D
Defense response
Immunoglobulin mediated immune response
Complement activation, classical pathway
Immune effector process
Synapse pruning
-log10(Pvalue)
Count
GeneRatio
E
Tyrobp
Trem2
C1qa
C1qc
C1qb
F
C1qa
C1qb
C1qc
Trem2
Tyrobp
Genotype
TG
WT
Normalised counts
Age (months)

Figure 4

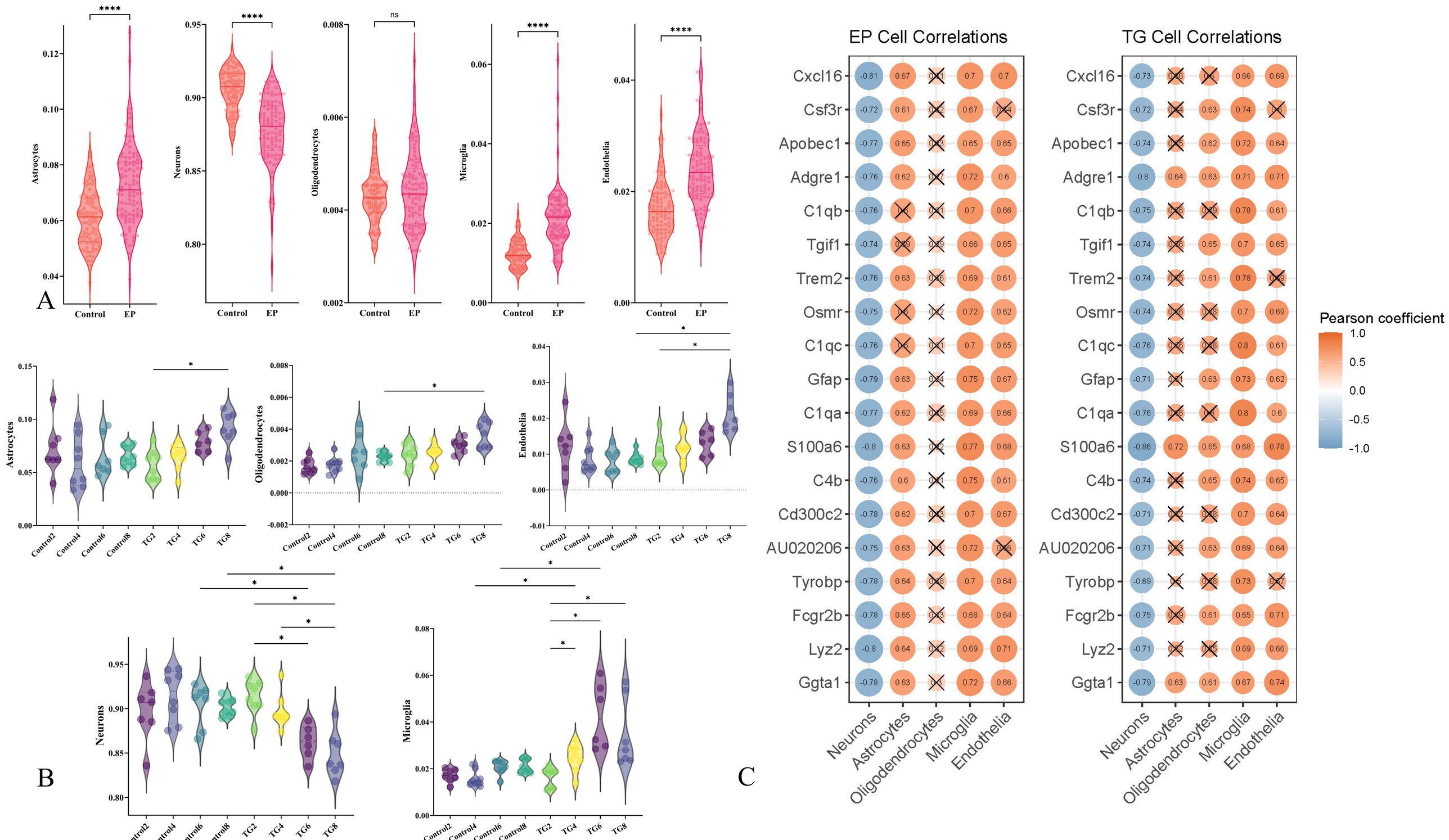
A
Astrocytes
Neurons
Oligodendrocytes
Microglia
Endothelia
Control
EP
****
ns
B
Control2
Control4
Control6
Control8
TG2
TG4
TG6
TG8
C
EP Cell Correlations
TG Cell Correlations
Cxcl16
Csf3r
Apobec1
Adgre1
C1qb
Tgif1
Trem2
Osmr
C1qc
Gfap
C1qa
S100a6
C4b
Cd300c2
AU020206
Tyrobp
Fcgr2b
Lyz2
Ggta1
Neurons
Astrocytes
Oligodendrocytes
Microglia
Endothelia
Pearson coefficient
1.0
0.5
0.0
-0.5
-1.0

Figure 5

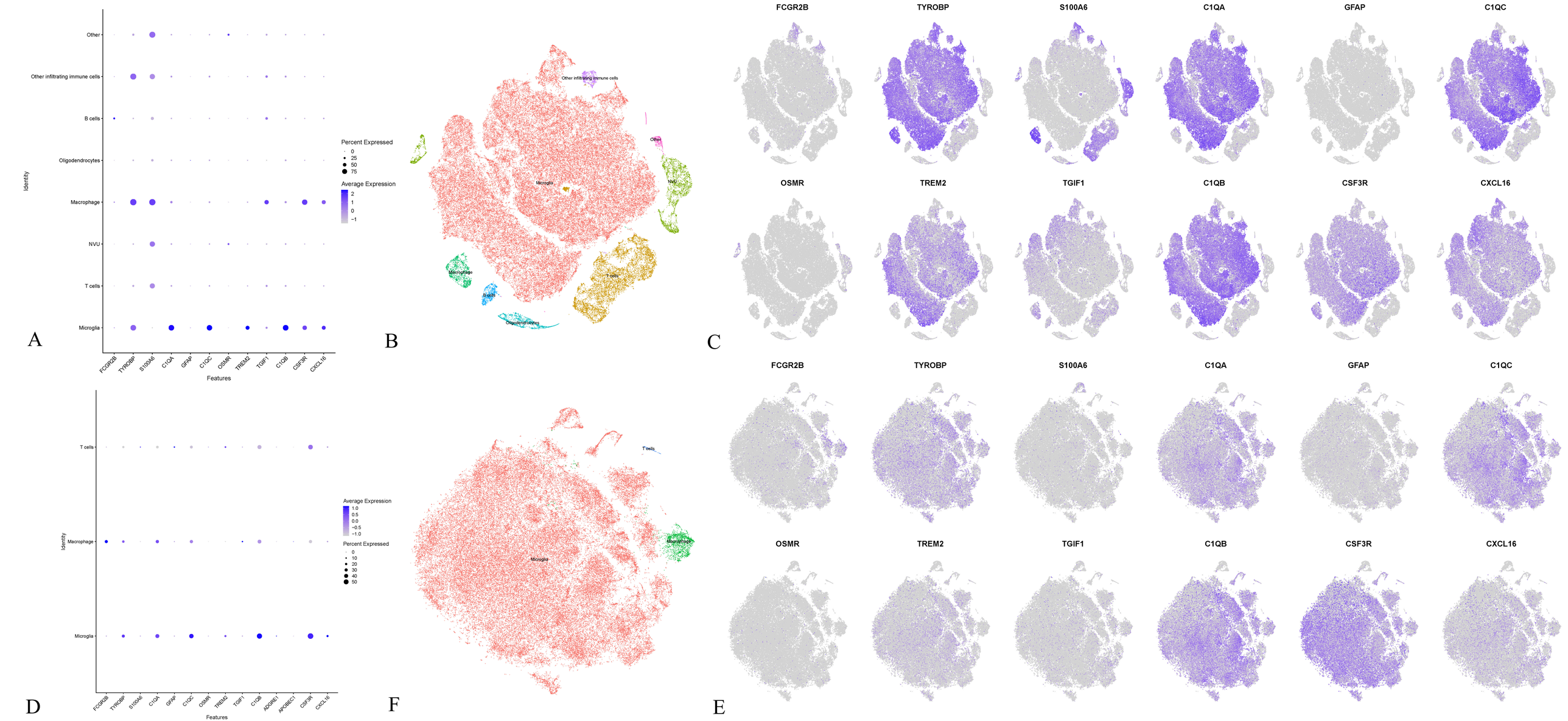
A
Other
Other infiltrating immune cells
B cells
Oligodendrocytes
Macrophage
NVU
T cells
Microglia
Identity
FCGR2B
TYROBP
S100A6
C1QA
GFAP
C1QC
OSMR
TREM2
TGIF1
C1QB
CSF3R
CXCL16
Features
Percent Expressed
0
25
50
75
Average Expression
2
1
0
−1
B
Other infiltrating immune cells
Other
Microglia
NVU
Macrophage
T cells
B cells
Oligodendrocytes
C
FCGR2B
TYROBP
S100A6
C1QA
GFAP
C1QC
OSMR
TREM2
TGIF1
C1QB
CSF3R
CXCL16
D
T cells
Macrophage
Microglia
ADGRE1
APOBEC1
Average Expression
1.0
0.5
0.0
−0.5
−1.0
Percent Expressed
0
10
20
30
40
50
F
T cells
Macrophage
Microglia
E
FCGR2B
TYROBP
S100A6
C1QA
GFAP
C1QC
OSMR
TREM2
TGIF1
C1QB
CSF3R
CXCL16

Figure 6